Breakdown of doublet recirculation and direct line drives by far-field flow in reservoirs: implications for geothermal and hydrocarbon well placement

R. Weijermars[1] and A. van Harmelen[2]

[1]*Harold Vance Department of Petroleum Engineering, Texas A&M University,* 3116 *TAMU College Station, TX* 77843-3116*, USA.*
E-mail: R.Weijermars@TAMU.edu
[2]*Department of Applied Mathematics, Delft University of Technology, Mekelweg* 4*, Delft* 2628*CD, The Netherlands*

SUMMARY

An important real world application of doublet flow occurs in well design of both geothermal and hydrocarbon reservoirs. A guiding principle for fluid management of injection and extraction wells is that mass balance is commonly assumed between the injected and produced fluid. Because the doublets are considered closed loops, the injection fluid is assumed to eventually reach the producer well and all the produced fluid ideally comes from stream tubes connected to the injector of the well pair making up the doublet. We show that when an aquifer background flow occurs, doublets will rarely retain closed loops of fluid recirculation. When the far-field flow rate increases relative to the doublet's strength, the area occupied by the doublet will diminish and eventually vanishes. Alternatively, rather than using a single injector (source) and single producer (sink), a linear array of multiple injectors separated by some distance from a parallel array of producers can be used in geothermal energy projects as well as in waterflooding of hydrocarbon reservoirs. Fluid flow in such an arrangement of parallel source-sink arrays is shown to be macroscopically equivalent to that of a line doublet. Again, any far-field flow that is strong enough will breach through the line doublet, which then splits into two vortices. Apart from fundamental insight into elementary flow dynamics, our new results provide practical clues that may contribute to improve the planning and design of doublets and direct line drives commonly used for flow management of groundwater, geothermal and hydrocarbon reservoirs.

**Key words:** Numerical solutions; Hydrology; Hydrothermal systems.

1 INTRODUCTION

The principal aim of our theoretical framework and flow visualizations is to increase awareness that far-field flow in reservoirs may lead to the progressive penetration and breakdown of doublets by a far-field flow. The first part of our study systematically investigates the breakdown of a point doublet (or singularity) and its natural extension, the spaced doublet. A doublet singularity with a superimposed far-field flow is commonly described by potential functions, originally used to model the flow around a perfect circular cylinder (Milne-Thomson 1962; Dalton & Helfinstine 1971). In the presence of a relatively slow far-field flow, doublet singularities will form a boundary that confines a cylindrical space where the far-field flow cannot enter or participate (Fig. 1). High resolution flow modelling of the doublet approximation for flow around a cylinder based on our analytical description reveals that assumptions about both the orientation and rate of the far-field flow are critical for maintaining integrity and size of the doublet flow space. More particular, the far-field flow orientation relative to the doublet polarity is critical for maintaining the integrity of the doublet and the far-field rate controls the size of the doublet flow space (see later in this study).

The fact that doublets are very sensitive to any far-field crossflow, which may lead to loss of closed-loop recirculation, has been little emphasized in concurrent literature. Our study reveals that the confined doublet flow space can be penetrated by a far-field flow, and may become leaky, in two different ways: (1) by gradually misaligning the orientation of the far-field flow direction with respect to the symmetry plane containing the two poles of the doublet singularity, and, when alignment is maintained and (2) by progressively increasing the far field flow rate due to which the doublet flow space confinement shrinks and gradually vanishes. Alternatively, a decreasing injection rate accomplishes the same.

An improved description of doublet flow is of practical importance, because the doublet is the archetypal well-design used for fluid recirculation in geothermal energy projects (Adams *et al.* 2015). Also for hydrocarbon extraction projects the doublet is a
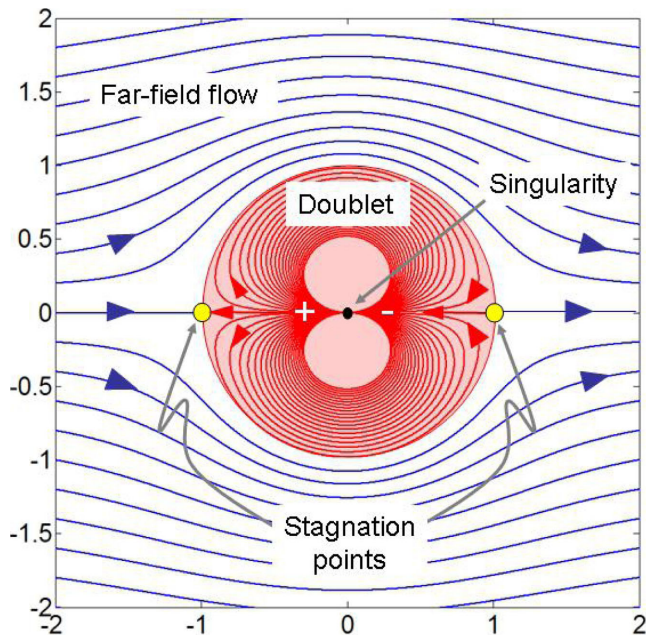
Figure 1. Flow paths tracked for far-field fluid (blue particles) and injection fluid (red particles). The doublet singularity has non-dimensional strength $m^* = 1$ and the far-field flow-rate $U_x^* = 1$. Upstream and downstream stagnation points are marked (yellow dots).

well-known configuration in, for example, reservoirs with heavy oil that require steam injection (Jelgersma 2007; Giacchetta *et al.* 2015). In such projects, any far-field flow will have a profound impact on recovery efficiency. However, far-field flow orientation and rate are commonly unknown and may remain unspecified. Our study shows that controlled flow management needs to account for the impact of the far-field flow on any doublet well pair (hence the importance of tracer pilot studies). When doublet breakdown develops, reservoir fluids may follow a flow path that completely deviates from that initially planned. In other words, a key concern should be whether the pair of injector and producer wells can establish the doublet flow as intended by well engineers, or will become affected by any far-field flow. An aspect only rarely (Holzbecher & Sauter 2010) or not at all emphasized in earlier studies, is that such details, in fact, determine whether the doublet may remain intact or will start to leak and break down over time.

We first model and visualize the progressive break down of singularity and spaced doublets and then proceed to model doublets made up of multiple sources and sinks such as used in a direct line drive. Additionally, we include examples of other geological features such as an impermeable fault and leaky fractures, which may disrupt the doublet flow. Particle movement paths are tracked with high resolution using algorithms based on superimposed potential functions using modern microprocessors. Particle paths thus tracked provide insight in the flow kinematics of superimposed flows when key parameters are systematically varied. This article is organized as follows. Section 2 embeds our research in the concurrent body of literature, outlining the model and its basic assumptions. Results for the breakdown of doublet singularities and spaced doublets by a far-field flow are given in Sections 3 and 4, respectively. Multiple doublet analysis and its approximation by a line doublet are detailed in Section 5. Results for line-doublet breakdown by a far-field flow are given in Section 6. Examples of doublet disruption due to other factors than a superposed far-field flow (such the presence of an impermeable fault or leaky fractures) are given in Section 7.

A brief discussion and conclusions are given in Sections 8 and 9, respectively.

2 PRIOR WORK, MODELLING METHOD AND ASSUMPTIONS

2.1 Prior work

Doublet flow can be modelled by potential theory superposing potential functions of a single source and sink, with or without a far-field flow (Milne-Thomson 1962; Kuethe & Chow 1998). Such models are accurate or approximate descriptions of natural flows, depending upon the similarity conditions. One practical use of doublet flow arrangements applies to reservoirs where injection fluid can be extracted with a higher heat content than the injected fluid. Such geothermal projects are ongoing in various countries around the world (Lund *et al.* 2004; Tomaszewska & Pajak 2012; Hirst *et al.* 2015; Røgen *et al.* 2015). Viable options for geothermal sites remain, including the transformation of depleted hydrocarbon fields into geothermal ones (Hirst *et al.* 2015; Soldo & Alimonti 2015); where both fields may be characterized by established and/or modified doublet flows.

Potential flow theory has been widely used to model Darcy flow dynamics, assuming irrotational flow in incompressible fluids. Among many applications are groundwater flow (Da Costa & Bennett 1960; Strack 1989; Holzbecher 2005), geothermal well doublets (Holzbecher & Sauter 2010; Holzbecher *et al.* 2011; Tomaszewska & Pajak 2012; Hirst *et al.* 2015; Røgen *et al.* 2015), aerodynamics (Kuethe & Chow 1998), hydrodnamics (Milne-Thomson 1962) and slow viscous creep of rock, mud flows, lava streams, ice glaciers and salt sheets (Weijermars & Poliakov 1993; Weijermars 2014, 2015; Weijermars & Van Harmelen 2014; Weijermars *et al.* 2014).

2.2 Assumptions in this study

For this study we assume a reservoir with Darcy flow, which means there are no inertia effects and the flow is creeping and fluid remains incompressible. Additionally, we assume that the injected fluids are homogeneous and the reservoir may range from homogeneous to various types of heterogeneity. In a homogeneous reservoir that has no heterogeneities, anisotropy or faults, Darcy flow of fluid through the pore space of a reservoir can be described with simple potential functions, yielding on a macroscopic level continuous streamlines that connect injection and production wells. Potential functions have been used extensively to model irrotational 2-D flow in incompressible fluids (Batchelor 1967). Creeping flow past a cylinder for example, can be modelled by potential functions by superposing a source, a sink and a far-field flow (Fig. 1). The 2-D reservoir description adopted in our study is a standard approach in reservoir modelling as detailed by us in a related study that benchmarks the streamline visualization code against an alternative method using two commercial software packages for reservoir simulation and a proprietary code from an industry sponsored consortium at TAMU (Weijermars *et al.* 2016). The latter study also demonstrates how our analytical flow code can be used to inversely model and distinguish the impact of heterogeneous subsurface features on the flow recirculation. We thus limit our attention to a 2-D flow description of 3-D reservoirs by assuming finite thickness and no vertical velocity gradients occur in the subhorizontal reservoir studied (a so-called 2.5 D approach, as 3-D fluxes in finite reservoir layers are accounted for).

The terms 'dipole' and 'doublet' are often times used indistinctively even in professional literature. In our study we consistently use the term doublet for the pairs of sinks and sources oriented according to the terminology definitions of the various analytical elements given and illustrated in Appendix A1. We distinguish between a doublet and dipole, and partly follow Strack (1989), but point out where his approach can be simplified (Appendices A2 and D). The term 'recirculation' is used throughout our study to avoid confusion with 'circulation', which in a mathematical sense refers to rotational flows. Our potential flow descriptions involve no superimposed vortex, so that the overall flow remains irrotational and accordingly the vorticity or the curl of the flow velocity should be zero; no vorticity implies no circulation.

Thermal effects are not explicitly included in our study. Heat from the ambient reservoir fluid can be transmitted to the doublet flow via one or several of the three following processes: advection, convection and/or conduction. In relatively thin aquifers convection is unlikely, and advection and conduction are considered the main mechanisms of heat transfer (Drange 2011; Doddema 2012; Hecht Mendez 2012; Bellini 2013). In the thin reservoir we assume, all thermal effects occur by either advection and/or diffusive conduction. For any particular case involving heat transfer with only a minimal effect on fluid viscosity, such as is the case for water or brine, the fluid recirculation pattern will not be affected. Holzbecher *et al.* (2011) showed the conductive heat transfer for one spaced doublet is largely dominated by advective heat transport along the stream lines of the fluid travel path. Our study visualizes the advection of the reservoir fluid towards the doublet, but we neglect conductive heat transfer. Building forward from insights of Holzbecher & Sauter (2010), we present algorithms that can be scaled for broader use in further systematic studies as well as in specific applications.

2.3 Flow visualization method

Figures in this study have been generated using Matlab. The code developed can trace individual streamlines as well as non-dimensional time contours, which is used in Section 7 showing the disruption of an advancing waterflood front at regular time increments. Tracing each streamline is accomplished by first choosing an initial position, z_0^* (using complex coordinates), from which the tracing starts at the non-dimensional time $t_0^* = 0$. Next one selects a non-dimensional time step, Δt^*. The position of the tracer at non-dimensional time t_1^*, that is after one non-dimensional time step Δt^*, is denoted by $z_1^*(t_1^*)$ and can now be calculated as:

$$z_1^*(t_1^*) = z_0^*(t_0^*) + v[z_0^*(t_0^*)]\Delta t^*. \tag{1}$$

In the above notation $v(z_0^*(t_0^*))$ is the velocity of the particle located at position z_0^* at non-dimensional time t_0^*. The velocity is calculated using complex vector field functions, which for the various doublet flows visualized in our study, are summarized in Appendices B–E. Smooth streamlines are obtained for small values of Δt^* (e.g. $\Delta t^* = 0.01$). However, a stronger injector (source), producer (sink) and/or far-field flow may require a smaller Δt^*. Generalizing this concept, the position of a tracer at non-dimensional time t_j^* is given by:

$$z_j^*(t_j^*) = z_{j-1}^*(t_{j-1}^*) + v[z_{j-1}^*(t_{j-1}^*)]\Delta t^*. \tag{2}$$

In the case of a doublet singularity, the injector and producer pipelines are hosted in the same drill hole (Fig. 2a) and the particle paths induced in the reservoir describe full circles (Fig. 2b). The typical doublet flow pattern possesses one symmetry plane that separates two flow half-spaces that do not exchange any fluid. Each half-space, at either side of the fluid separation plane, is occupied by perfectly circular streamlines of increasing radii (Figs 2b and d). Although line integrals can be solved to find the particle paths (or streamlines when steady state) we additionally in our study track fluid particles to find their position at regular time intervals and construct time-of flight contours (such as included in Figs 13, 19 and 20). Such contours are different from the potential surfaces and cannot be found using solely an integral method. The source strengths may be time-dependent (e.g. see Weijermars *et al.* 2014) and we can still track the particle paths correctly as the potential flow solution at each instant gives the instantaneous streamlines and the time-series of solutions at each instant enables us to track the resulting particle paths. To apply this approach inertia effects should remain absent, which is the case in slow groundwater flow and a prerequisite for Darcy flow.

2.4 Singularity and spaced doublets

The flow of a single doublet under various far-field flow angles has been previously investigated (Da Costa & Bennett 1960). Holzbecher & Sauter (2010) illustrate how quickly the flow regime becomes complex by show-casing the flow-field using up to three spaced doublets in a far-field flow and, additionally, also systematically illustrate the impact of the far-field flow angle on the flow regime. Our study shows for both the spaced doublet as well as the singularity doublet how the closed-loop recirculation is affected by both the far-field flow angle and flow rate.

When separate wells are drilled with a finite spacing between the injection and production well (Fig. 2c), the particle paths are no longer complete circles but become stretched circle segments (Fig. 2d). The cylindrical doublet model can thus be expanded to include flow past an elongated Rankine body (Fig. 3); flow past a cylinder (Fig. 1) is only an end-member of a continuous series of solutions. We demonstrate that the fluid recirculation in cylindrical and Rankine flow spaces will progressively disrupt when the original fluid separation plane (with positive pole pointing upstream) rotates away from the far-field flow direction. An increase of the angle between the baseline of the well pair and the direction of the far-field flow leads to progressive breakdown of the cylindrical and Rankine flow domains (Sections 3 and 4).

We introduce the terms 'antipolar' and 'polar' alignment with far-field flow. Antipolar alignment means the far-field fluid particles that travel in a straight line towards the upstream stagnation point will reduce to zero speed in the stagnation point and are met at the other side of that stagnation point by fluid particles with a reverse velocity maintaining the internal recirculation of the doublet (Fig. 4a). Polar alignment means the internal recirculation at the horizontal symmetry axis of the doublet is fully aligned with the direction of the far-field flow; the injector and producer are positioned such that central flow due to internal recirculation is not counter to the far-field flow but in the same direction (Fig. 4b). For this case, the stagnation points are no longer aligned with the far-field flow direction; the inter-connector of the two stagnation points occurs at 90° with respect to the far-field flow direction. The derivation of the flow stagnation points and other relevant algorithms can be found in Appendices B1–B3.

2.5 Multiple doublets

The flow pattern of doublets becomes more complex when multiple doublets are drilled in, for instance, high-temperature geothermal fields (Adams *et al.* 2015). Accurate or approximate visualizations and control of the subsurface flow are of key importance for
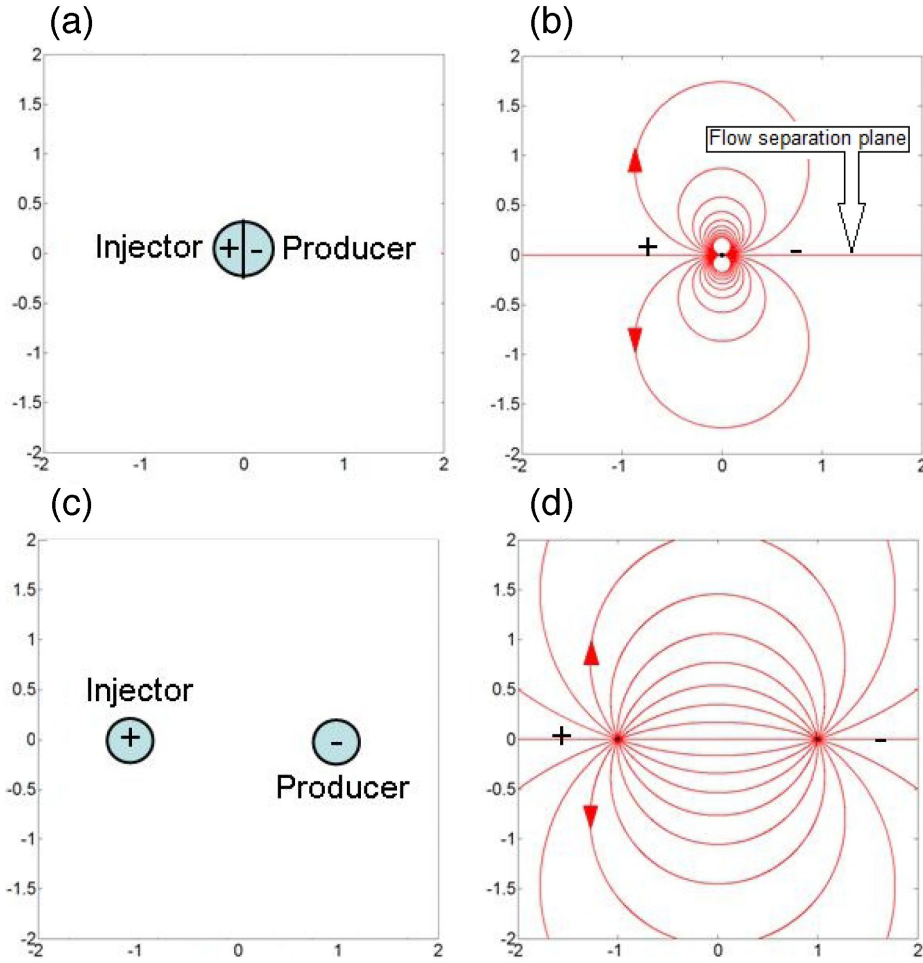
Figure 2. Particle paths for doublet singularity or point doublet (a) and spaced-doublet (b). Injector is a source (marked by +) and producer is a sink (marked by −). There are no flow stagnation points in the absence of a far-field flow.
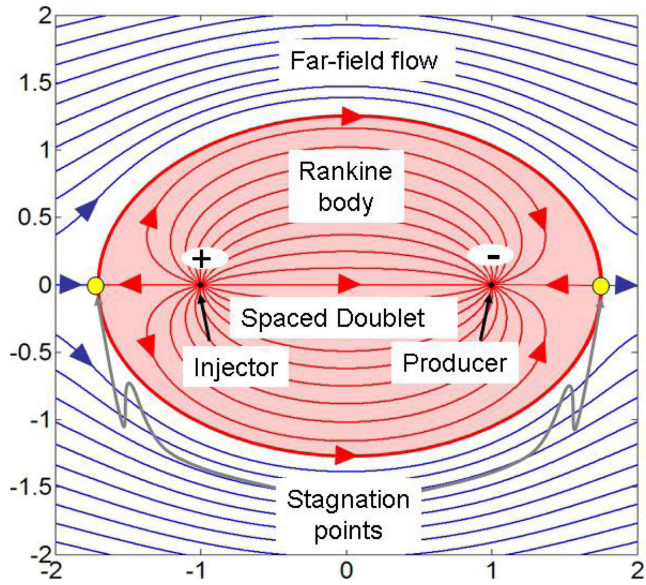

Figure 3. Rankine body outlines effective sweep region for injection fluid (red curves). Well strengths of the doublet's injector and producer pair are constant and equal: $m^*_{injector} = +1$ and $m^*_{producer} = -1$. Rankine body region is flattened by far-field flow-rate $U_x^* = 1$.

efficient recovery of any advective geothermal energy, especially because of the possible interaction of producer and injector wells with the far-field flow aquifer flow. Our study investigates and visualizes the progressive breakdown of multiple source and sinks in parallel arrays in the presence of a far-field flow by systematically varying the strength of the far-field relative to the direct line drive. We demonstrate that a direct line drive array composed of a linear array of point injectors and producers in an unconstrained reservoir can be approximated by a line doublet to represent the macroscopic flow field (Section 5). The line doublet approach gives some computational gain. The crucial point is that the two flows are macroscopically identical, but the effect of the far-field flow on the stagnation point migration is more straightforward to compute than when different point sources and sinks are used.

Potential functions of line doublets provide analytically accurate and physically approximate descriptions of natural flows, applying kinematic similarity conditions. The three basic well patterns visualized in Figs 5(a)–(c) all make use of specific complex potentials that provide closed-form solutions which allow high-resolution tracking of particle paths (see Section 2.4). The flow lines for unperturbed singularity and spaced doublets are visualized in Figs 5(a) and (b) (left-hand side). When a far-field flow is superimposed such that it remains aligned with the baseline of an injection and a production well placed downstream (so-called antipolar orientation, a term coined in our study, for details see Section 2.4), the singularity

(a) Antipolar alignment Far field

(b) Polar alignment Far field
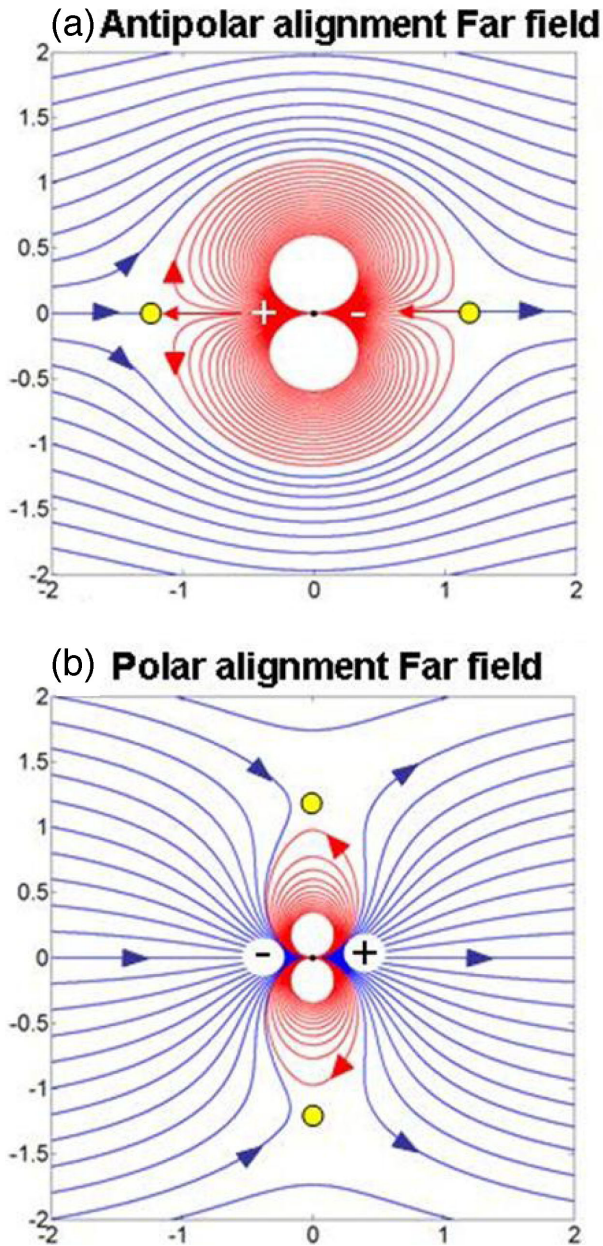
Figure 4. (a) Antipolar alignment of doublet poles with far -field flow. (b) Polar alignment of doublet poles with far- field flow. Note the different positions of the stagnation points (marked by yellow dots) for each case.

doublet develops internal recirculation confined to a cylindrical flow domain (Fig. 5a, right-hand side). Similarly, the spaced doublet in antipolar alignment with the far-field flow (Fig. 5b, left-hand side) develops a flow pattern where the injected fluid remains confined to a Rankine body, which is an oval flow domain with the long ellipse axis oriented parallel to the direction of the far-field flow (Fig. 5b, right-hand side). The first part of our study systematically investigates the conditions that lead to the breakdown of singularity doublets (Fig. 5a) and spaced doublets (Fig. 5b) when a superposed far-field flow occurs in the subsurface reservoir.

The second part of our study (Sections 5 and 6) analyses how a far-field flow in a model reservoir may result in the breakdown of the constrained flow domain occupied by a line doublet (Fig. 5c). The line doublet is an elementary flow arrangement that concisely

represents an array of injectors and producers in direct line-drive arrangement. When a line doublet (made up, for example, by a horizontal well that is hosting both the injection and production tubes with multiple perforations; Fig. 5c, left-hand side) is subjected to a superposed far-field flow, an oval flow domain forms in case of an antipolar doublet orientation (Fig. 5c, right-hand side). The direction of the long ellipse axis, measured from the centre of the line doublet, typically depends on the length and strength of the line doublet as well as the strength of the far-field flow (Fig. 5c, right-hand side). For instance a line doublet orthogonal to the far-field flow direction can maintain internal recirculation confined to a transverse oval flow region (Fig. 5c, right-hand side), which distinguishes the line doublet's internal recirculation from the Rankine body (Fig. 5b, right-hand side).

In a final part of this study we incorporate an impermeable fault in the reservoir (Section 7). The potential function for including this fault has been derived using conformal mapping (see Appendix E), which make it possible to visualize flow past impermeable surfaces in the reservoir while maintaining the continuity condition. We resort to conformal mapping solution rather than the method of images (*cf.* White 2011), because the former method (unlike the method of images) is not constrained by a requirement of impermeable boundaries that act as symmetry planes for the ambient flow. The detailed results of our various flow visualizations are systematically discussed in the following sections.

3 RESULTS FOR DOUBLET SINGULARITIES

3.1 Doublet singularity aligned with far-field flow (variable U_x^*)

The doublet singularity (Fig. 2b) will evolve into a perfect cylindrical flow space when subjected to a far-field flow, but only when the two stagnation points remain aligned with the far field flow direction and the injector (positive pole) of the doublet is pointing upstream, so-called antipolar alignment (Fig. 6a). The first effect highlighted here is the progressive shrinkage of the cylindrical flow space occupied by the injection fluid when the far-field flow rate increases (Figs 6a–d). Superposition of a far-field flow on the unperturbed doublet singularity of Fig. 2(b) results in the creation of two stagnation points, which come from 'infinity' and then move towards the eye (centre) of the doublet when the far-field flow-rate becomes stronger relative to the doublet strength (Figs 6c and d).

The flux per unit area of the doublet is progressively faster when the far-field flow-rate increases, because the far-field flow supports the internal recirculation of the fluid entrapped in the doublet singularity. The internal recirculation is supported via external advection along the periphery of the cylindrical flow space which itself is driven by the pressure of the injector and producer wells.

For practical situations, where the far-field flow-rate in a subsurface reservoir is unknown, or unresolved at the scale required for accurate well management, the sweep of the injection fluid through the reservoir may become ineffective. This occurs when the far-field flow-rate is much faster than anticipated (or if it was wholly neglected in the original well-plan). The sweep region of the doublet is reduced by the impact of the far-field flow and thus becomes less effective. The area of the sweep region occupied by the cylindrical flow-space is dependent on the relative rates of the far-field flow U_x^* and the doublet strength m^*. The radius, r, of the swept region
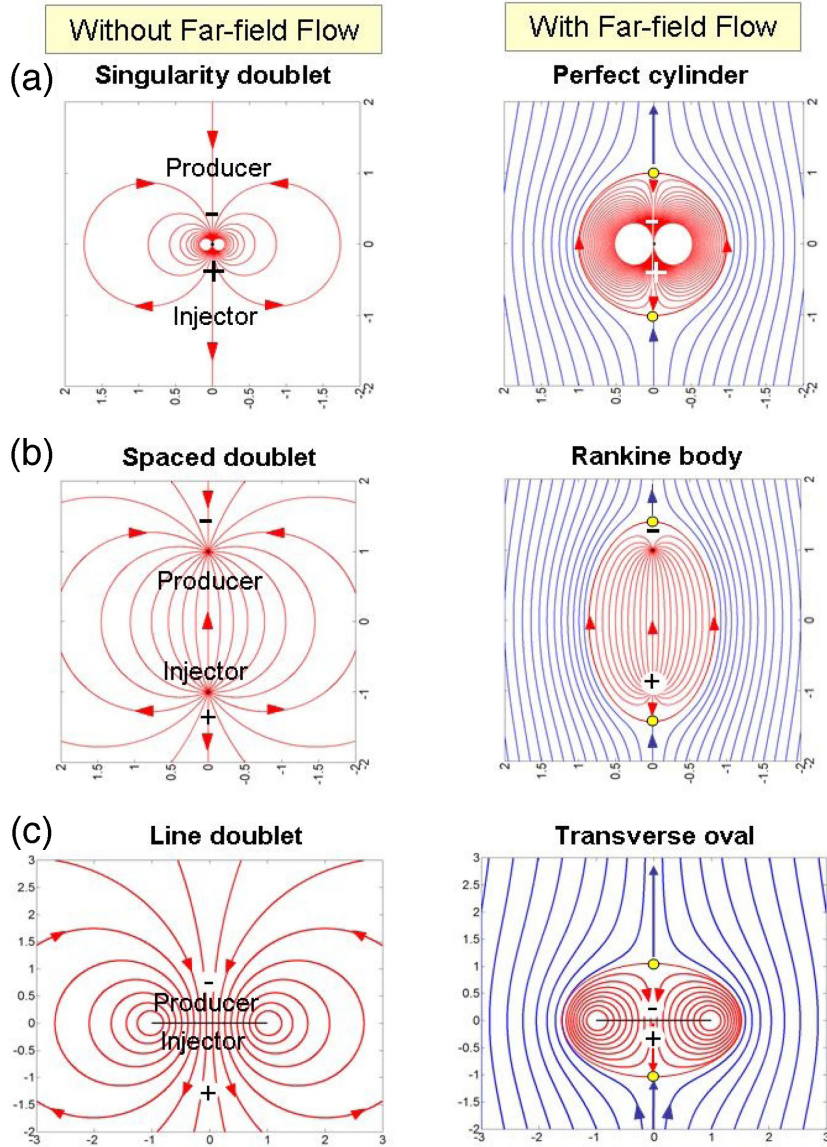
Figure 5. Left-hand side: particle paths tracked for (a) perfect doublet singularity or point doublet, (b) spaced doublet and (c) line doublet. Injector is a source (marked by +) and producer is a sink (marked by –). There are no flow stagnation points in the absence of a far-field flow. Right-hand side: flow paths for all three cases with injection fluid (red particles) tracked with superposed far-field fluid (blue particles) in antipolar alignment with doublets. The source has non-dimensional strength $m^* = 1$ and the far-field flow-rate $U_y^* = 1$. Upstream and downstream stagnation points are marked (yellow dots).

(i.e. the radius of the cylindrical flow space) corresponds to half the separation distance of the two stagnation points:

$$r = \sqrt{\frac{m^*}{U_x^*}}. \tag{3}$$

With $m^* = Q^*/2\pi h^*$, where Q^* is the 3-D flux of the source and h^* the characteristic thickness of the layer. The radius of the region effectively drained by the doublet will vanish when $U_x^* \gg m^*$, as follows from Eq. (3) and by extrapolating to infinity the series of solutions displayed in Figs 6(a)–(d). The residence time of the injection fluid in the reservoir diminishes as far-field strength increases or pump rate (m) decreases. Counter-intuitively, faster pump rates would allow longer residence time than slower pump rates (argument only valid for antipolar alignment) allowing for higher conductive heat transfer in geothermal reservoirs and larger sweep areas in hydrocarbon reservoirs. For conversion of non-dimensional

quantities to dimensional units, comprehensive scaling rules are given in Weijermars & Schmeling (1986).

3.2 Doublet singularity misaligned with far-field flow (constant U_x^*)

A second significant cause of effective distortion of the doublet flow space occurs when the original symmetry-axis of the doublet singularity becomes misaligned with respect to the far-field flow direction. Any misalignment of the connector between the injector (recharger) and producer (extraction) with the far-field flow direction will result in a rotation of the stagnation points (Figs 7a–f). The misalignment will immediately lead to loss of the original cylindrical shape of the doublet singularity. The doublet symmetry is restored when the injector and producer are again aligned with the far-field flow direction (Fig. 7f) but now $180°$ rotated with respect to their original polarity (Fig. 7a). The two extremes for sweep
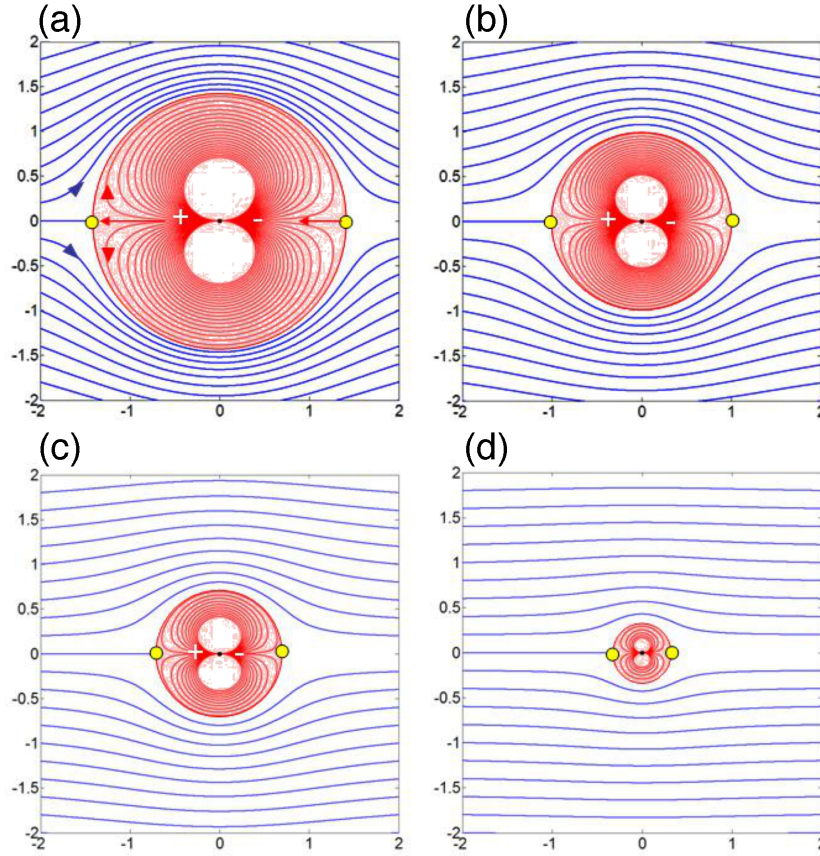
Figure 6. Flow paths tracked for far-field fluid (blue particles) and injection fluid (red particles). The point doublet has equal strength in all four cases illustrated (a–d: $m^* = 1$), but the far-field flow-rate increases from a to d as follows. (a) $U_x^* = 0.5$; (b) $U_x^* = 1$; (c) $U_x^* = 2$, and (d) $U_x^* = 10$. Upstream and downstream stagnation points are marked (yellow dots).

effectiveness are as follows. Maximum sweep area is occupied by the doublet of a given strength for antipolar alignment with the far-field flow (Fig. 7a). Minimum sweep area occurs for the same doublet strength and the same far-field flow for polar alignment (Fig. 7f).

Also, the flux per unit area of injection fluid is progressively faster when the fluid separation plane of the doublet and the injector at the upstream side of the cylinder progressively rotate away from the far-field flow direction (Figs 7b–f). The subsurface recirculation of the fluid (which is injected into the doublet at a constant rate in all cases) becomes faster, because the stagnation points rotate away from the flow direction when the doublet becomes misaligned with the far-field flow. Consequently, the far-field flow will progressively contribute more effectively to the internal recirculation of the doublet. Part of the far-field fluid is produced, and part of the injected fluid becomes part of the far-field flow. The subsurface area occupied by doublet fluid diminishes when the misalignment between the doublet axis and far-field flow increases.

flow space and passes through the eye of the singularity. Fig 8(a) shows that a part of the far-field fluid is produced and a part of the injection fluid is never recovered as it becomes part of the far-field flow. The doublet for such cases pumps a mixture of far-field fluid and injected fluid, and the relative fluxes along the sets of stream tubes are colour coded in Figs 7(b)–(e). This assumes the far-field fluid does not diffuse into the injection fluid.

It is clear from the above synthetic models of doublet flow patterns that systematic conceptual knowledge about the recirculation rates is crucial for the successful development of both geothermal wells and hydrocarbon wells. We contend that sophisticated flow simulations are performed by industry. Nonetheless, apart from a groundbreaking study Holzbecher & Sauter (2010), we are not aware of any other systematic discussion of the doublet breakdown (point doublet and doublets with spaced wells). The effects illustrated above provide significant additional insight to aid well design and ensure well orientation remains in optimum alignment with any far-field flows – and the respective recirculation rates of the injector and producer wells should be determined accordingly.

3.3 Doublet singularity misaligned with far-field flow (variable U_x^*)

An increase in the far-field flow-rate leads to a shrinkage of the area swept by the injected fluid (Figs 6a–d). This effect also occurs in the case of the misaligned doublet (compare Figs 8a and b). About equal (half) volumes of the injection fluid will circulate in each of the recirculation loops. The far-field flow enters the doublet

4 RESULTS FOR SPACED DOUBLETS

4.1 Spaced doublet (Rankine body) aligned with far-field flow (variable U_x^*)

We next model the effect of a far-field flow superposed on the spaced-doublet of Figs 2(c) and (d). When the far-field flow remains perfectly aligned with the symmetry axis of the unperturbed
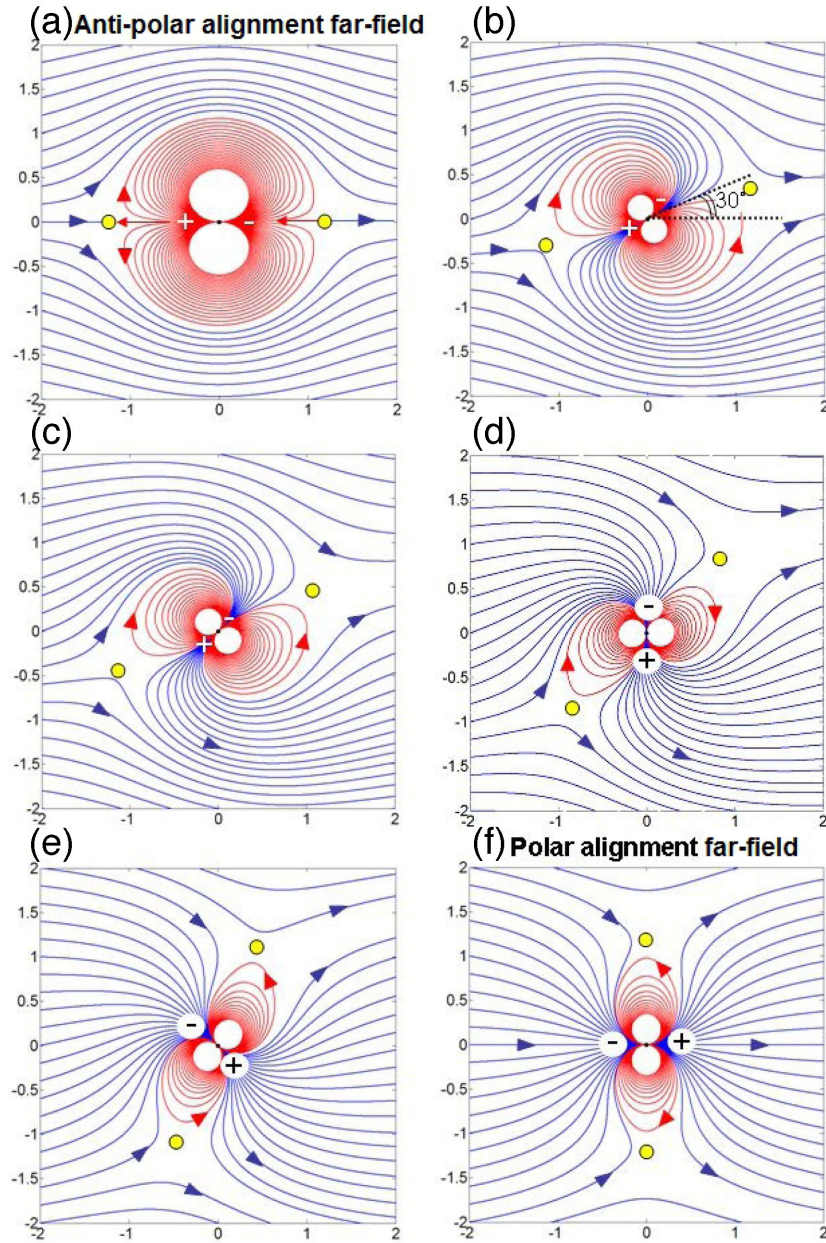
Figure 7. Travel paths tracked for far-field fluid (blue curves) and fluid injected at the doublet recharger (red curves). Stagnation points are marked in yellow. Far-field flow-rates and doublet strengths are kept constant in all simulations (a–f); $U_x^* = 1$ and $m^* = \sqrt{2}$. The different flow patterns are entirely due to rotation of the doublet axis (or fluid separation plane): (a) $0°$, (b) $30°$, (c) $45°$, (d) $90°$, (e) $135°$ and (f) $180°$ (rotation is positive in anticlockwise direction). Upstream and downstream stagnation points also rotate when the doublet becomes misaligned with respect to the far-field flow direction.

spaced-doublet flow, the doublet develops a Rankine body (Fig. 9). All the injected fluid is contained in the space occupied by the Rankine body, which outlines the area swept by the injection fluid. Faster far-field flow-rates lead to more slender envelope shapes of the Rankine oval (Figs 9a–d). The sweep area is effectively compressed by faster far-field flow-rates and would ultimately reduce to a straight line segment between the injector and producer well when the far-field flow-rate is infinity large with respect to the strengths of the wells. The maximum width of a Rankine half-body for one well is given by (White 2011):

$$N = \frac{2\pi m^*}{U_x^*}. \tag{4}$$

4.2 Spaced doublet (Rankine body) misaligned with far-field flow (constant U_x^*)

When the two spaced wells (injector and producer) are no longer aligned with the direction of the far-field flow, the Rankine body ceases to exist (Figs 10b–e). As the Rankine body breaks down, a portion of the fluid volume from the injector well never reaches the production well. The production well will produce a mixture of injection fluid and far-field fluid; only a fraction of the original injection fluid appears in the production well. When the injection well is located downstream of the far-field flow direction (so-called polar alignment), none or only a negligible fraction of the injection fluid may reach the producer (assuming the far-field flow is sufficiently strong; Fig. 10e). For any case where the spaced doublet has
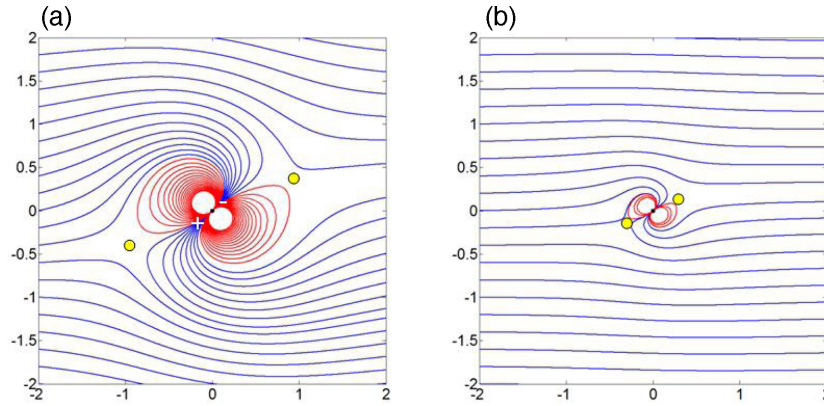
Figure 8. Doublet axis is oriented at 45° to the far-field flow direction. The well strength is constant ($m^* = 1$) for both cases (a) and (b), but far-field flow rate is for (a) $U_x^* = 1$ and (b) $U_x^* = 10$. The sweep area of the doublet (red recirculation) is reduced accordingly.
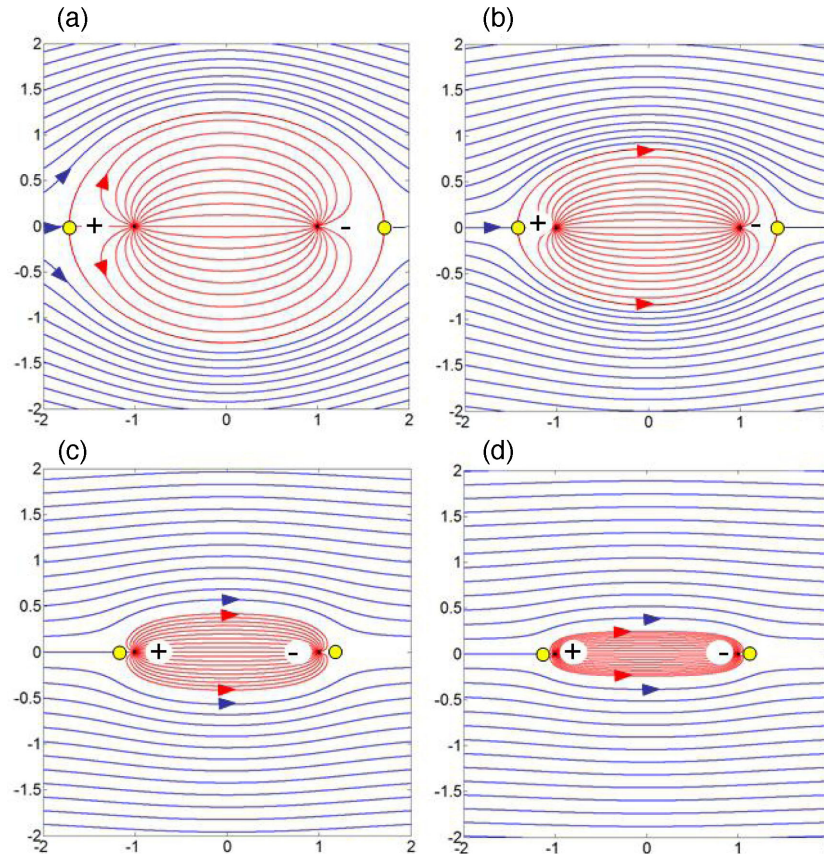
Figure 9. Rankine body outlines effective sweep region for injection fluid (red curves). Well strengths of the doublet are constant and equal for all cases ($m^*_{injector} = +1$ and $m^*_{producer} = -1$). Rankine body region is flattened by faster far-field flow-rates: (a) $U_x^* = 1$; (b) $U_x^* = 2$; (c) $U_x^* = 5$, and (d) $U_x^* = 10$.

no longer a Rankine body shape, a large area intended to be swept by the injection fluid is no longer benefitting the producer well. Most of the injection fluid sweeps away from the producer well, particularly when the production well is located further upstream from the injection well (Fig. 10e).

The loss of sweep fluid will be even more dramatic when the far-field flow-rate is already relatively high as compared to the well rates of the doublet (Figs 11a–d). When the doublet angle (tilt of the line between injector and producer) is just 10° relative to the far-field flow direction, only half of the injection fluid is effectively sweeping the doublet region (Fig. 11b). When the angle is increased to 15°, sweep efficiency of the injection fluid is further reduced to about 1/10th of the original doublet space (Fig. 11c). When the doublet tilt angle is increased to 20° or more, all injection fluid will be lost and no longer contributes any sweep for the producer well (Fig. 11d).

The effects of the far-field flow on the fluid recirculation of the spaced doublet have been systematically visualized. The above results confirm that optimum alignment with any far-field flow direction is crucial for better sweep efficiency and well injection rates should be fast enough to mitigate any undue flattening of the Rankine flow-space.
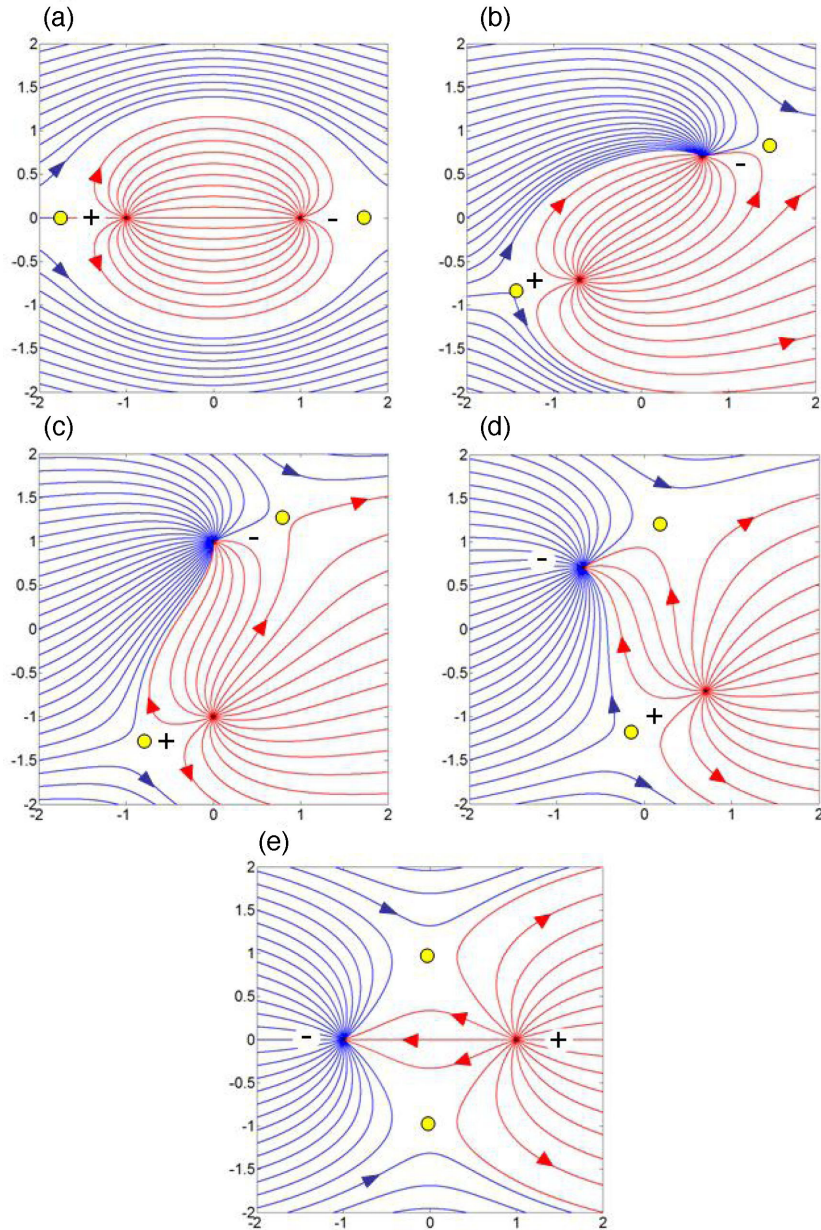
Figure 10. Progressive misalignment of well doublet base-line with far-field flow direction. All rates are constant ($m^*_{injector} = +1$, $m^*_{producer} = -1$, and $U_x^* = 1$). A progressively larger volume of injection fluid is lost and entrained in the far-field flow. Rotation of the doublet base-line is: (a) 0°, (b) 45°, (c) 90°, (d) 135° and (e) 180°.

## 5 MULTIPLE DOUBLET ARRAYS PROXIED BY LINE DOUBLET

5.1 Direct line drive array; macroscopic and magnified top views

A macroscopic top view of an unconfined reservoir penetrated by a direct line drive composed of a lower linear array of injectors and an upper linear array of producers is given in Fig. 12(a). More specifically, the flow field contains 20 spaced doublets, existing of pairs of point sources and point sinks. The streamlines visualized in Fig. 12(a) develop when the flow (resembling a line doublet) is not perturbed by a far-field flow. Fig. 12(b) illustrates the effect of a far-field flow, which confines the recirculation of the injection fluid to a transverse oval flow space similar to that seen in Fig. 5(c,

right-hand side image). The central area of Figs 12(a) and (b) show a flow pattern that is identical to that of a direct line drive array. The streamlines inside the central area, that is in-between doublet pairs, appear as approximately straight lines, though the outermost pairs of spaced doublets connect streamlines that display a slight curvature. However, on the scale of Fig. 12(a) it is difficult to see what is exactly happening in-between the doublet pairs, which is why Fig. 13 shows a detailed flow simulation for the direct line drive region in the central portion of Fig. 12(a) using a reduced number of doublet pairs.

The direct line drive of Fig. 13 visualizes the streamlines (blue) in the flow space between the injectors and producers as well as the non-dimensional time contours (red) using five pairs of injectors and producers. The non-dimensional time contours mark the progression front of injection fluid, using a marker line initially located
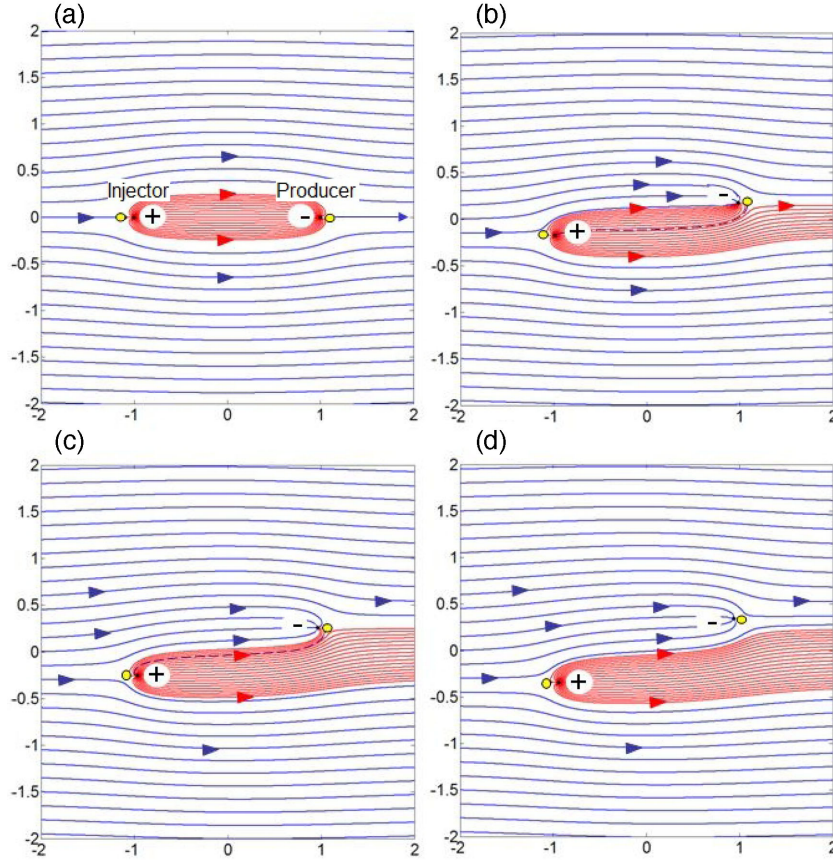
Figure 11. Effect of sweep efficiency rapidly reduces when the baseline of a Rankine doublet is tilted with respect to the direction of a relatively fast far-field flow. The far-field flow-rate ($U_x^* = 10$) is in this simulation superposed onto a constant doublet pair ($m^*_{injector} = +1$; $m^*_{producer} = -1$). (a) Perfect Rankine sweep occurs when tilt is $0°$; (b) only about half of the injected fluid reaches the producer well for a baseline tilt of $10°$. Dashed line separates upper injection fluid moving towards producer well and lower half of the injected fluid moving downstream with the far-field flow; (c) only 1/10th of the injection fluid sweeps into the producer for a baseline tilt of $15°$; (d) none of the injection fluid reaches the producer well when the doublet baseline tilt is $20°$ or more.
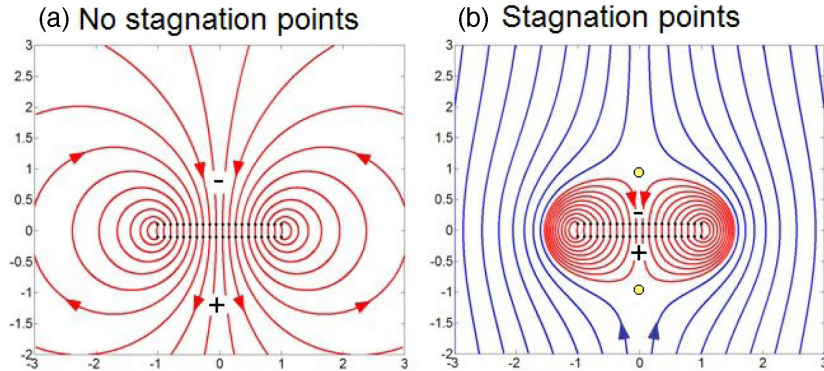

Figure 12. Line dipole approximations by arrays of point sources and sinks consisting of 20 point sources equally spaced from $-1 - \varepsilon i$ to $1 - \varepsilon i$ with strength $m^* = \frac{1}{2\varepsilon}\frac{2}{20}$ and 20 point sinks equally spaced from $-1 + \varepsilon i$ to $1 + \varepsilon i$ with strength $m^* = \frac{1}{2\varepsilon}\frac{-2}{20}$ and $\varepsilon = 0.1$. (a) Without far-field flow. (b) With superposed far-field flow (blue; antipolar-alignment) of strength $U_y^* = 1$. Stagnation points are marked in yellow.

just above the injectors at the onset of the non-dimensional time clock used in our study.

The fluid of the innermost injector, I_3, will arrive earliest at its associated producer, P_3, before any of the other producers are reached by the fluid injected via the stream tubes originating from the corresponding injectors. Injection fluid from I_3 first reaches producer P_3, after which producers P_2 and P_4 are next reached by injection fluid from I_2 and I_4. The two outer producers are reached last by the injected fluid. This behaviour is indeed what one expects of a line drive. Fluid originating from the innermost injector experiences the same pressure from the two doublet pairs to the left as from those to the right and consequently experiences the steepest pressure gradient which pushes the fluid forward along almost straight lines. Moreover, this not only explains why the innermost streamlines are nearly straight lines, but also that fluid originating from a more outlying injector travels along more curvy streamlines, because such an injector has a non-symmetrical distribution of doublet pairs on its left- and right-hand sides and thus experiences curved
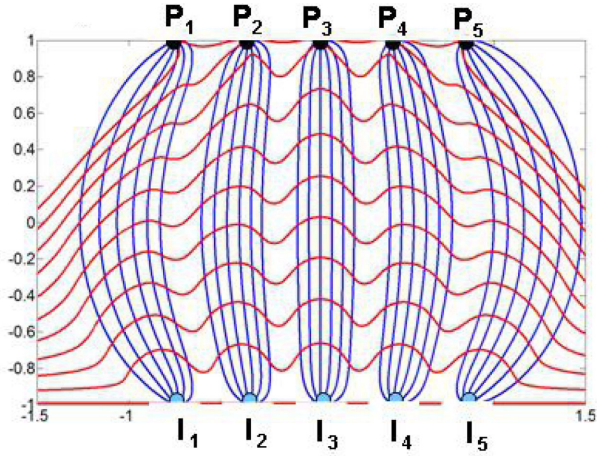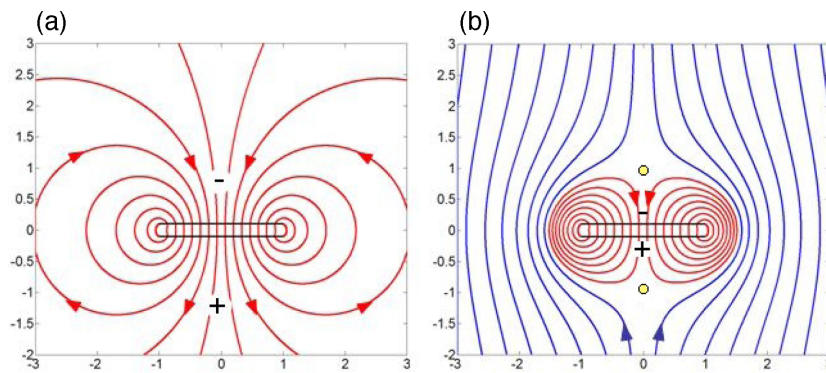
Figure 13. Direct line drive composed of a linear array of 5 injectors (I_1–I_5) and 5 producers (P_1–P_5). Streamlines in blue and displacement of horizontal marker line is outlined by red time of flight contours.

pressure potential lines. The (slight) curvature of the direct line drive's streamlines in Fig. 13 is also visible in Fig. 12(a); streamlines in-between each of the 20 doublet pairs appear as straight lines except for the outer two pairs, where a slight curvature occurs.

5.2 Spaced line source and line sink as a proxy for a direct line drive array

A series of spaced well doublets (or linear array of point sources and sinks) can be represented by a continuous line source and line sink (also respectively called interval source/sink; Potter 2008). Fig. 14 shows such a flow field for a continuous line source and line sink, both with an equal and uniform strength distribution. In Fig. 14(a) the red contours describe the flow paths of the injected fluid. Comparing the flow domain of Fig. 14(a) with Fig. 12(a) confirms the flow patterns are identical, though different streamlines are tracked. The mathematical details of a line source description are given in Appendix C1.

For Fig. 14(b) again the familiar transverse oval flow domain appears, due to the superposition of a uniform far-field flow onto the spaced line source and line sink in antipolar orientation. The far-field fluid is coloured blue, whereas the injected fluid is consistently dyed red. The flow patterns of Figs 14(b) and 12(b) look similar, although different streamlines are tracked (just as Fig. 14a and 12a). Near the tips of the line source and line sink however, curved streamlines

occur not unlike those seen in Fig. 13. For both Figs 14(a) and (b) we conclude that indeed the combination of a spaced line-source and line sink is a viable proxy for a direct line drive on a macroscopic level.

5.3 Line doublet as a proxy for direct line drive array

The next step is to further simplify our line drive description by closing the distance in-between the spaced line source and line sink to zero, that is to let ε go to zero. The mathematical approach to accomplish this is analogous to that used for creating a singularity doublet from a spaced doublet which we detailed in Appendix B1. Appendix C2 in this study details how to obtain the line doublet from singularity doublets.

Fig. 15 depicts the flow field for a line doublet. A comparison of the flow domains of Figs 14(a) and 15(a) (where no far-field flow is present), as well as Figs 14(b) and 15(b) (where a far-field flow is superimposed), reveals that they are practically identical, again with the exception that different streamlines have been tracked. Therefore, the comparison reveals that on a macroscopic level a line doublet can fairly accurately replace the spaced line source and line sink as a proxy for a direct line drive.
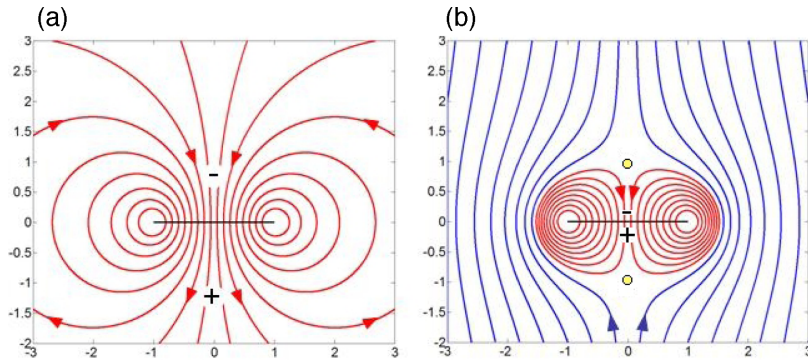
6 RESULTS FOR LINE DOUBLETS

Using the approximation of a direct line drive by a line doublet as a starting point (Section 5), we show in the remainder of this study how a far-field flow in a reservoir can destroy a direct line drive. The collapse of the intended direct line drive may occur in two ways: (1) by a strong far-field flow in antipolar alignment with the internal recirculation of the line doublet and (2) by a progressive misalignment of the far-field flow with respect to the fluid separation plane of the line doublet. The breakdown of the direct line drive is detailed in the next two sections using the macroscopically equivalent line doublet as a valid proxy.

6.1 Line doublet in antipolar alignment with far-field flow direction (variable U_y^*)

Fig. 16 shows the progressive breakdown of the line doublet by a far-field flow, which faces the positive side of the line doublet head on (antipolar alignment), under increasing strength of the

Figure 14. Direct line drive approximation made up of an equally strong line source (+) and line sink (–). Line source located from $-1 - \varepsilon i$ to $1 - \varepsilon i$ with strength $m^* = 2/2\varepsilon$ and line sink located from $-1 + \varepsilon i$ to $1 + \varepsilon i$ with strength $m^* = -2/2\varepsilon$ and $\varepsilon = 0.1$. (a) Without far-field flow. (b) With superimposed far-field flow (antipolar alignment with direct line drive) of strength $U_y^* = 1$. Stagnation points are marked in yellow.

Figure 15. Line doublet as macroscopic proxy for a spaced line source and line sink. Line doublet is located from $-1 + 0i$ to $1 + 0i$ with strength $m^* = 2$. (a) Without a far-field flow. (b) With a superimposed far-field flow (antipolar alignment) of strength $U_y^* = 1$. Stagnation points are marked in yellow.
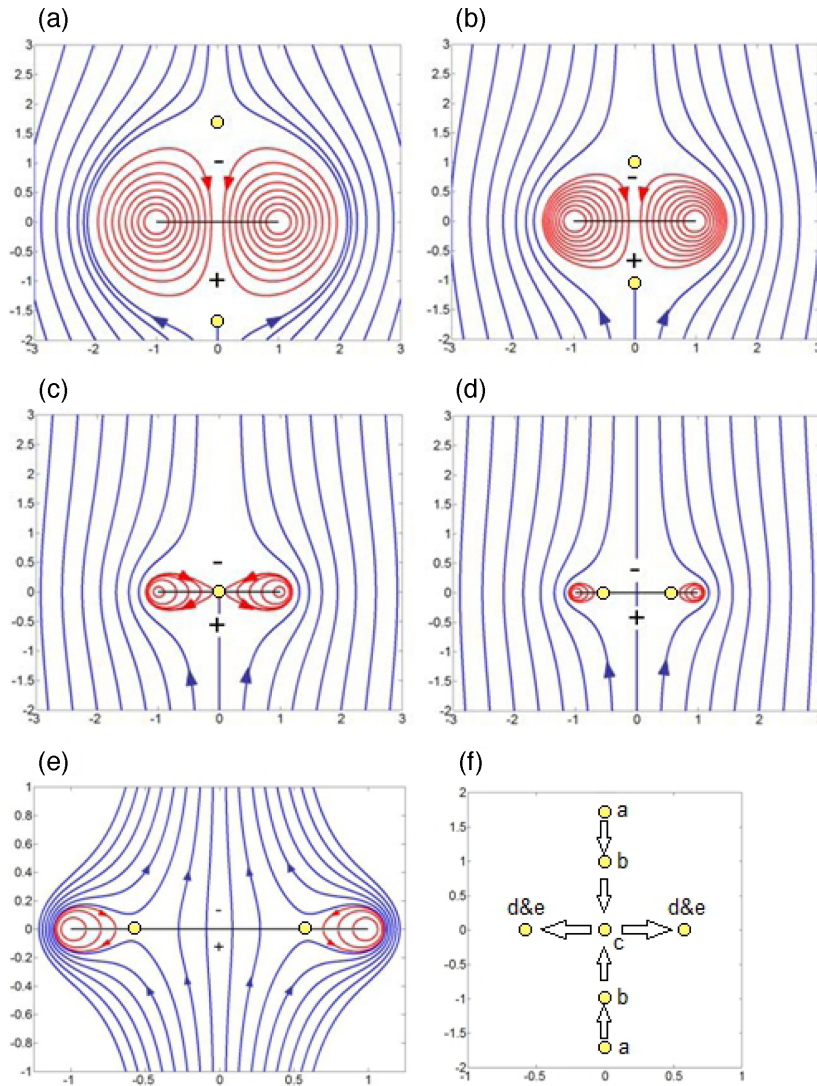
Figure 16. Progressive breakdown of line doublet of strength $m^* = 2$ (antipolar alignment of doublet poles with respect to far-field flow) with centre at the origin. Endpoints located at $-1 + 0i$ and $1 + 0i$. (a) Far-field flow strength $U_y^* = 0.5$. (b) Far-field flow strength $U_y^* = 1$. (c) Far-field flow strength $U_y^* = 2$. (d) Far-field flow strength $U_y^* = 3$. (e) Zoom of (d), showing the breakup of the line doublet. (f) Progression of the stagnation points. Lettered stagnation points correspond with those of figures (a)–(e).

far-field flow with the strength of the line doublet kept constant. The circulatory flow of fluid due to the line doublet is shown in red, whereas far-field flow lines are shown in blue. Stagnation points are depicted as yellow dots with a black boundary. When the ratio of far-field flow strength to line doublet strength increases, the injected fluid develops into a lemniscate (Fig. 16c) and eventually separates into two vortices resembling Cassinian ovals (Figs 16d and e). We note the overall flow is irrotational, as the two vortices

have equal magnitudes but opposite sign that cancel, which leaves zero vorticity at the far-field boundaries (infinity).

Initially, the two stagnation points are some distance away from the doublet plane and their connector is normal to that plane (Fig. 16a). When the far-field flow becomes stronger, the stagnation points progressively move closer to the line doublet (Fig. 16b). When the lemniscate develops, the two stagnation points coincide and there is just one stagnation point separating the two vortices of the lemniscate (Fig. 16c). The two initial stagnation points of Figs 16(a) and (b) have in the specific stage of Fig. 16(c) been reduced to a single stagnation point, however, the far-field fluid does not yet flow through the lemniscate of the line doublet. The lemniscate develops when the following condition is fulfilled (see Appendices C3 and C4):

$$(z_a - z_b)^2 = 4 \cdot m^*/U_y^*. \tag{5}$$

Expression (5) uses z_a and z_b as complex coordinates for, respectively the left- and right-hand tips of the line doublet. A lemniscate will develop if the line doublet length squared equals 4 times the relative strength of the line doublet and far-field flow rate.

However, when the far-field flow grows still stronger, the lemniscate will break apart into two vortices resembling Cassinian ovals. Figs 16(d) and (e) show the far-field strength has overpowered the line doublet's strength and once again two stagnation points appear, though this time they both lie on the line doublet and far-field fluid then breaks through the line doublet section between those stagnation points. The location of the stagnation points, z_{sp}, can be found by solving the equation $V(z) = 0$. Using α and β for, respectively the far-field flow and line doublet orientation (in radians), solving $V(z) = 0$ yields (see Appendices C3 and C4):

$$z_{sp} = \frac{z_a + z_b \pm \sqrt{(z_a - z_b)^2 + 4\frac{im^*}{U_y^*}e^{(\alpha+\beta)i}}}{2}. \tag{6}$$

The shifting positions of the stagnation points when the far-field strength increases are plotted in Fig. 16(f).

A far-field flow relatively weak as compared to the line doublet will result in two (mobile) stagnation points initially situated far away from the line doublet. These stagnation points move towards the line doublet when the relative strength of the far-field flow increases. Once touching the line doublet, each of the stagnation points moves in opposite direction, normal to the far-field flow, and is attracted by the two vortices. At very high far-field flow rates the fluid recirculation becomes separated by a wide zone of penetrating far-field fluid from the aquifer.

6.2 Line doublet misaligned with far-field flow direction (variable U_y^* and m^*)

We next show the impact on the streamlines in the reservoir when the far-field flow direction and the line doublet (proxying for the direct line drive) are oriented parallel. Rotating the line doublet by 90° in counter-clockwise direction (Fig. 17) predictably has a significant effect on the flow pattern. Because the line doublet is no longer in antipolar orientation, part of the far-field fluid will always be drawn into the line doublet. The amount of entrained far-field fluid however, depends on the length of the line doublet as well as on the angle and strength of the line doublet with respect to the far-field's orientation and strength.

Fig. 17(a, left-hand column) shows the flow regimes resulting when a line doublet of constant strength $m^* = 2$ is oriented parallel to the far-field flow direction and subjected to increasing

far-field flow strengths. Fig. 17(a, top figure) uses a far-field flow relatively weak compared to the line doublet, which causes the strongest swirling effect on the far-field flow fluid in the entire series shown in Fig. 17(a). Since there is a strong swirling effect near the line doublet, the internal recirculation of the doublet (visualized as red lines) is occupying a relatively large subsurface area and the stagnation points, marked yellow, are farthest away from the line doublet's tips. Doubling the far-field strength (Fig. 17a, second row) has a strong effect on the flow pattern as the swirling and area of internal recirculation decreases and the stagnation points move closer to the tips of the line doublet. Continuing to the bottom two figures of Fig. 17(a), we see that the far-field fluid is, for the most part, blasted past the line doublet. Additionally, most of the far-field fluid that does end up at the line doublet no longer experiences the swirling effect. Another consequence is that the area of internal recirculation diminishes even further and the stagnation points occur almost on top of the well doublet's tips.

Fig. 17(b) is complementary to Fig. 17(a), which shows flow fields for varying line doublet strengths and constant far-field flow strength $U_y^* = 0.5$. The strength of the line doublet relative to the far-field flow strength increases from Fig. 7(b, top to bottom). The top figure in Fig. 17(b) is the same as in Fig. 17(a), but we zoomed out to visualize more of the surrounding area. Progressively doubling the strength of the line doublet causes more of the far-field fluid to travel towards the line doublet. Moreover, analogous to what occurs in Fig. 17(a), the reservoir area occupied by the doublet's internal recirculation increases (Fig. 17b, top to bottom). The doublet's influence gets stronger evermore and because of this the stagnation points move away from the line doublet. The increase of the line doublet's internal recirculation rate causes a stronger streamline jetting effect, that is the increasing amount of far-field fluid that reaches the line doublet is forced to flow through an increasingly narrower part of the line doublet causing streamlines to narrow their spacing more and more. Hence a streamline jetting effect occurs as fluid will move faster in such zones.

7 OTHER SOURCES OF DOUBLET DISRUPTION

In the above we have established systematic insight of direct line drive interaction with a far-field flow, which is but one mechanism that may led to the disruption of the fluid's closed-loop recirculation. Alternatively, geological attributes such as an impermeable fault and leaky fractures may cause severe distortion of the direct line drive's flow. Some examples have been illustrated in Weijermar *et al.* (2016). Further examples are elaborated below. We developed a practical approximation to simulate flow across high conductivity cracks and, alternatively, leaky fractures (see Appendix A2 and D). Leaky fractures in our study imply loss of reservoir fluid due to a sink flow normal to the plane of view, which is likely to occur in dilational fractures (Ferill & Morris 2003). We next apply these flow elements to hypothetical, but common tectonic settings including geological structures that may affect the flow of direct line drives.

7.1 Geological settings

Tectonic basins form when shallow crustal zones become deformed and fractured between tectonic plates moving at different speeds and/or in different directions (Weijermars 1993, 1998; Fossen 2010). Fluid flow in any reservoirs hosted in such basins may be affected by numerous structural features, such as shear faults (often
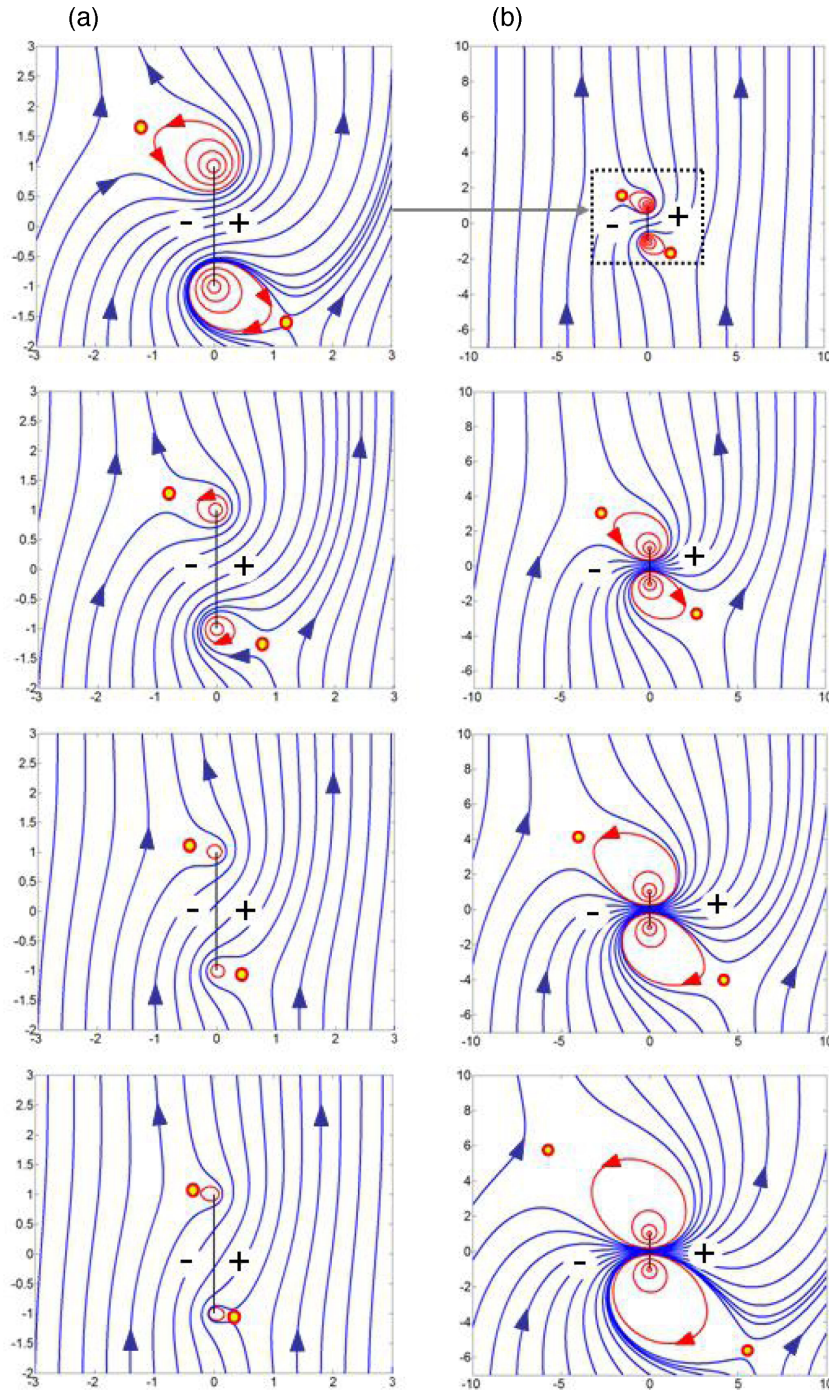
Figure 17. Doublet's leakage and stagnation points. Each line doublet has length 2 and angle 90° with respect to the origin. (a) Constant line doublet strength $m^* = 2$. Far-field flow strength is equal to (from top to bottom) $U_y^* = 0.5$, $U_y^* = 1$, $U_y^* = 2$ and $U_y^* = 3$. (b) Constant far-field strength $U_y^* = 0.5$, whereas line doublet strength equals (from top to bottom) $m^* = 2$, $m^* = 4$, $m^* = 8$ and $m^* = 16$.

impermeable due to clay smear and fault gauge; Twiss & Moores 2000) and dilation cracks or joints (often acting as either high conductivity fractures and/or leaky fractures; Strack 1989). Two principal examples of basins with such structural features and the position of a hypothetical direct line drive are sketched in Fig. 18. This simplified setup is used to further develop our analytical model of the direct line drive to visualize the impact on the flow pattern of a leaky fracture and an impermeable fault surface. Examples of geothermal projects located in compressional basin setting (as in Fig. 18a) which may contain such structural elements affecting the doublet

flow occur in the Basin and Range province (Faulds *et al.* 2012) and Sarulla graben (Hickman *et al.* 2004). Numerous geothermal projects are located in extensional basin settings (Fig. 18b) such as in the African rift valley (Omenda & Teklemariam 2010), Rhine graben (Houwers *et al.* 2015), Larderello rift (Bertani *et al.* 2006), Dixie Valley (Barton *et al.* 1997), Icelandic rift zones (Bjornsson & Hersir 1981) and Taupo Volcanic Zone (Rowlands & Sibson 2004; Rosenberg *et al.* 2009). The subsurface flow in all such basins will likely be affected by the detailed structures and conductivities of fractures and faults (Browne 1978; Onacha *et al.* 2010; Nukman &
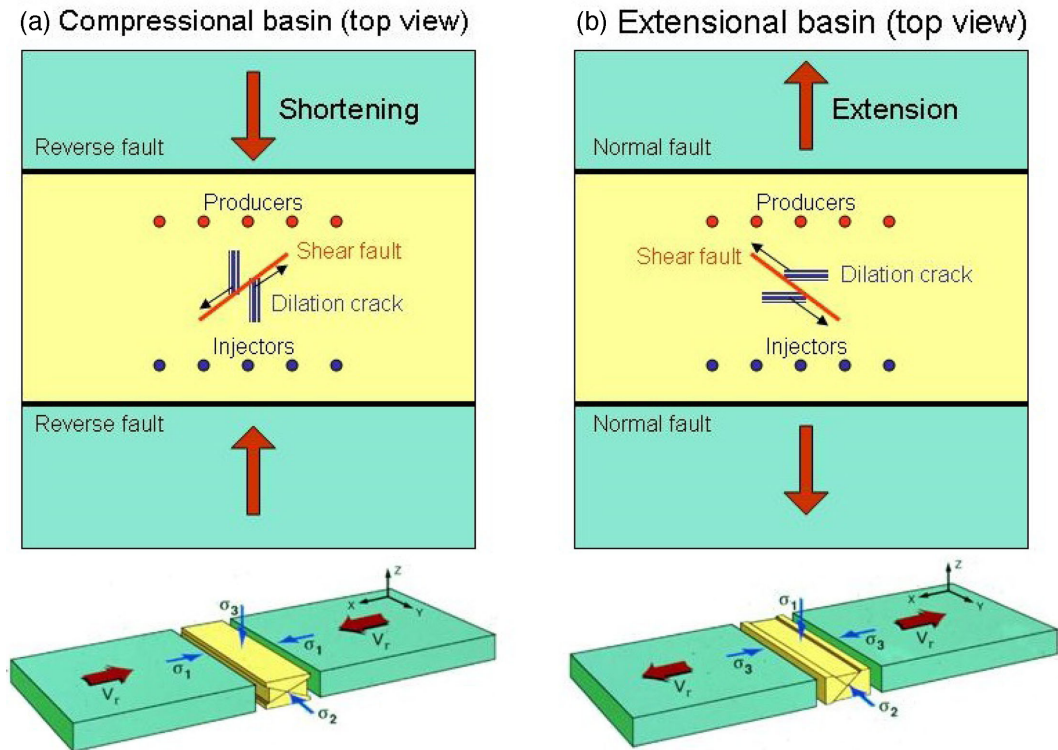
Figure 18. Top views of sedimentary basins with direct line drive flow region disrupted by an impermeable shear fault and a pair of leaky fractures (cracks). Shown are two principal settings (a) compressional basin, and (b) extensional basin. Bottom images show corresponding 3-D views, related plate motion vectors, V_r, and principal stress orientations, $\sigma_1, \sigma_2, \sigma_3$ (after Weijermars 1993).

Moeck 2013), which requires the development of a detailed reservoir model based on reservoir characterization and fluid migration modelling. Our study may help generate generic conceptual insight in how the doublets in such reservoirs may be affected by certain flow attractors (leaky fractures) and deflectors (impermeable faults).

7.2 Direct line drive array model with an impermeable fault and leaky fractures

The influence of one impermeable fault (see Appendix E for the derivation of the complex vector field functions) and two leaky fractures (Appendix D) on a flow field consisting initially of a direct line drive of five injectors (I_1 to I_5, all of strength $m^* = 1$) and five producers (P_1 to P_5, all of strength $m^* = -1$) without the presence of a far-field flow is given in Figs 19(a)–(d). An undisturbed direct line drive array is visualized in Fig. 19(a) where injected fluid is traced by blue streamlines and non-dimensional time contours mark the progression front of injection fluid in red. The marker line initially is located just above the injectors at the onset of the non-dimensional time clock used in our study.

As soon as an impermeable fault is introduced in the reservoir, Fig. 19(b), the flow pattern changes drastically. Importantly, an impervious boundary can be mapped by the method of images (White 2011) but this requires symmetry of the flow at either side of the boundary. A more versatile method makes use of conformal mapping (Appendix E). Because of the fault, fluid injected by injector I_3 is redirected from producer P_3 to P_4. Consequentially, fluid originating from injector I_4 is redirected to P_5 and fluid from injectors I_1 and I_2 is partially redirected to producers P_2 and P_3. Since the net strength of all injectors and producers is zero and no far-field flow is present, those streamlines in Fig. 19(b) that no longer reach

producer P_5 (because streamlines from injector I_4 were redirected to P_5) shall eventually reach one or more of the other producers. Although the flow pattern of the direct line drive is redirected by the impermeable fault, in essence the direct line drive remains intact.

The introduction of a leaky fracture in Fig. 19(c), through a linear array of ten point sinks with cumulative strength $m^* = -1$, drains fluid from the reservoir before it can reach any of the producers P_1 to P_5. Part of the fluid injected by three of the five injectors (I_2 to I_4) never reaches a producer but instead is removed from the reservoir by the leaky fracture. This is visualized by particles paths from injectors I_2, I_3 and I_4 which no longer flow around the impermeable fault but instead end up in the leaky fracture (Fig. 19c). Consequentially some of the fluid of injectors I_1 and I_2 that reached producers P_1 and P_2 (Fig. 19b), is redirected to producers P_2 and P_3 (Fig. 19c). This in turn leaves producer P_1 with none of the original particles traced in Fig. 19(a), suggesting that producer P_1 produces reservoir fluid. Since the net strength of point sources and point sinks in Fig. 19(c) is negative (–1), more fluid is removed from than added to the unconstrained reservoir. The leaky fracture removes part of the fluid injected by injectors I_2 to I_4 from the reservoir, due to which at least some of the producers receive less effective sweep. The direct line drive pattern of Fig. 19(c), although distorted by the leaky fracture, remains reasonably intact.

Next a second leaky fracture is introduced, again through a linear array of ten point sinks with cumulative strength $m^* = -1$, but this time located on the other side of the impermeable fault (Fig. 19d). Logically, this second fracture exacerbates the situation of Fig. 19(c) even further. Where the flow regime of Fig. 19(c) was quite similar to that of Fig. 19(b), the flow pattern of Fig. 19(d) is less similar to Fig. 19(b). Comparing Fig. 19(d) with Figs 19(a)–(c), only one of the traced streamlines originating from injector I_1 reaches a producer
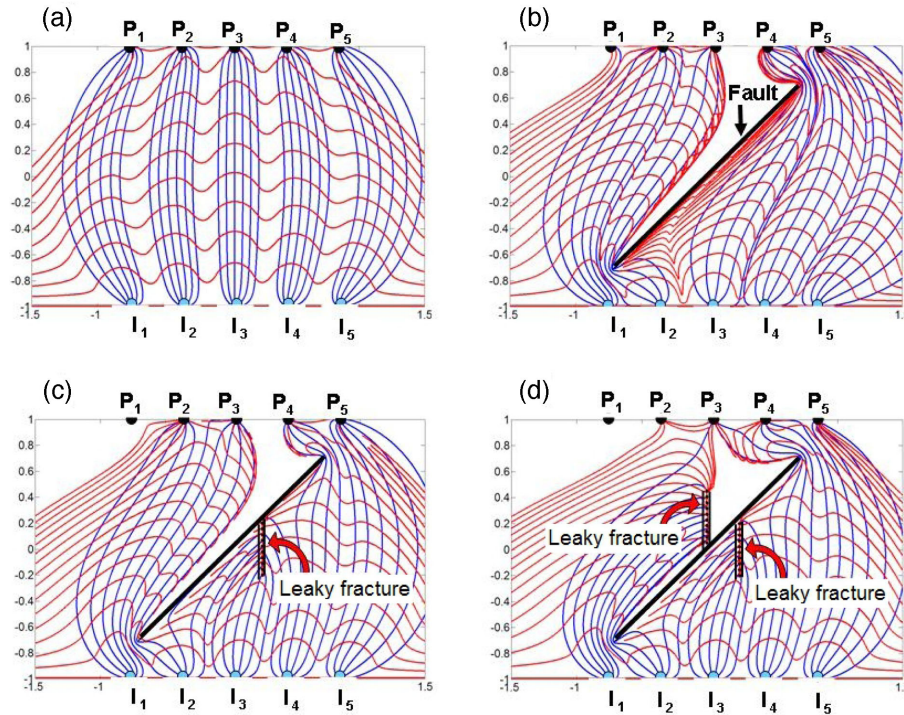
Figure 19. Progressive distortion of flow-field by means of impermeable and leaky fractures. Five injectors equally spaced from $-0.75 - i$ to $0.85 - i$ and 5 producers equally spaced from $-0.75 + i$ to $0.85 + i$. Each injector has strength $m^* = 1$ and each producer $m^* = -1$. No far-field flow is present. Flow lines visualized in blue and non-dimensional time contours visualized in red. Non-dimensional time spacing between contours: $t^* = 0.025$. (a) No faults are present. (b) Impermeable fault added with centre at the origin and angle $\beta = 45°$. (c) Leaky fracture added: 10 point sinks equally spaced from $0.25 - 0.2i$ to $0.25 + 0.2i$, each with strength $m^* = -0.1$. (d) Second leaky fracture is added: 10 point sinks equally spaced from $0 + 0.05i$ to $0 + 0.45i$, each with strength $m^* = -0.1$.

in Fig. 19(d). Due to the second leaky fracture specific streamlines reach producer P_3 (Fig. 19d) instead of producer P_2 (Fig. 19c). Moreover, some of the streamlines that in Fig. 19(c) were produced by producer P_4 and P_5 are now produced by producers P_3 and P_4, respectively (Fig. 19d). The introduction of the two leaky fractures, on opposite sides of the impermeable fault, has a significant effect on the direct line drive pattern.

In Fig. 20 the angle of the impermeable fault is now 135° (measured counter-clockwise from the injector baseline), which leads to Fig. 20(a) being analogous to Fig. 19(b), but horizontally mirrored. Adding the first and second leaky fracture, now oriented horizontally instead of vertically, the flow field resembles those of Figs 19(c) and (d). The first leaky fracture affects mainly the centre flow region of the direct line drive, whereas the second leaky fracture distorts one specific side of the direct line drive pattern. As the second leaky fracture lies on the right-hand side of the impermeable fault, it is the right-hand side of the direct line drive pattern that is affected most by the fracture. Step by step some of the producers no longer produce the in Fig. 19(a) originally traced particles, because many of these particles disappear via the leaky fractures.

8 DISCUSSION

8.1 Single doublet breakdown

This study has important implications for well-architecture planning and production efficiency in both geothermal energy and hydrocarbon extraction projects. Our analysis shows that when an aquifer background flow occurs, doublets will rarely retain closed loops of

fluid recirculation. When the far-field flow rate increases relative to the doublet's internal recirculation rate, the area occupied by the doublet will diminish and eventually vanishes. More fundamentally, when the baseline of the well pair making up the doublet is misaligned with respect to any far-field flow direction, the closed-loop recirculation of the doublet breaks down and its flow space will be penetrated by the far-field fluid. Doublets with rapid fluid recirculation allow little penetration by the ambient fluid when the far-field flow-rate is relatively slow. In contrast, slowly circulating doublets with fast far-field flow rates will entrain increasingly larger volumes of the ambient far-field fluid into their pumped recirculation. The presence of a far-field flow can be established by tracer studies in field pilot studies (Datta-Gupta & King 2007; Bjarkason 2014), which may then give dimensional inputs for the far-field flow rate and dominant direction in a particular full-scale field development project.

8.2 Multiple doublet breakdown

A direct line drive is one of the most simple and common arrangements for water flooding of hydrocarbon reservoirs, using a linear array of injectors separated by some distance from a parallel array of producers. Such arrangements are also used in geothermal energy projects. This study shows flow patterns of a direct line drive arrangement can be approached by a line doublet. The aim of our study is to model and visualize the progressive leakage of a line doublet when distorted by a far-field flow. An antipolar oriented line doublet can maintain a closed-loop recirculation of injection fluid under certain conditions. Nevertheless, it is possible for such a line doublet to break down under high far-field flow rates
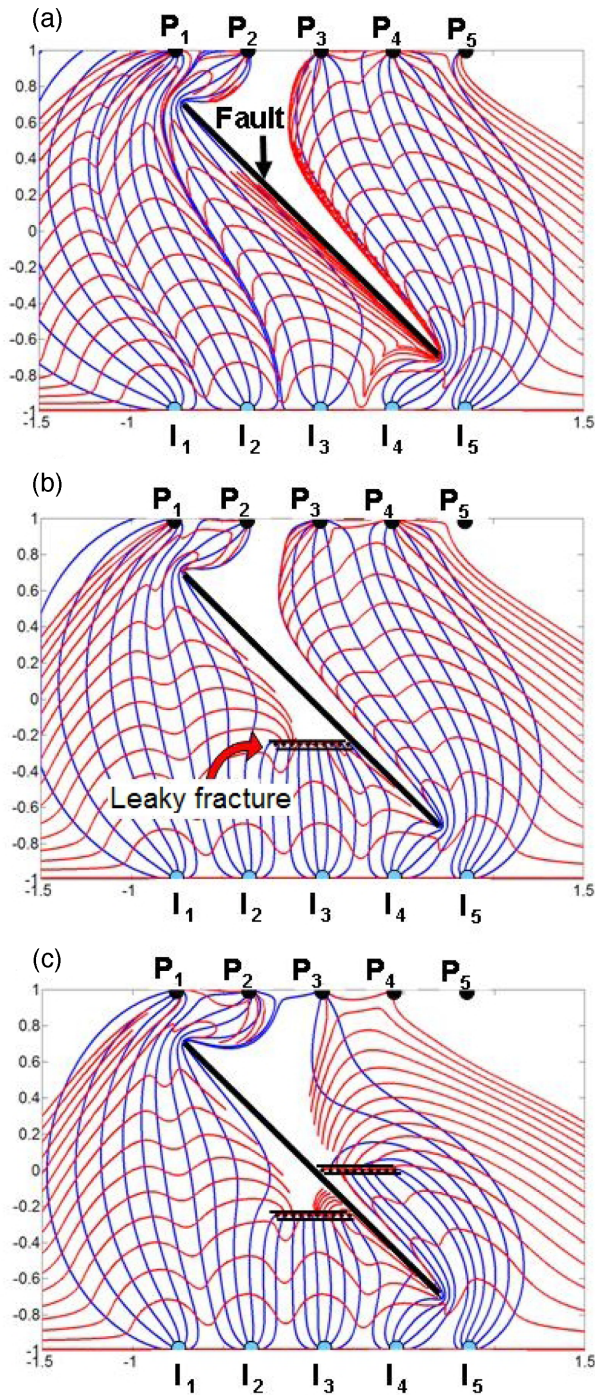
Figure 20. Progressive distortion of flow-field by means of impermeable and leaky fractures. Five injectors equally spaced from $-0.75 - i$ to $0.85 - i$ and 5 producers equally spaced from $-0.75 + i$ to $0.85 + i$. Each injector has strength $m^* = 1$ and each producer $m^* = -1$. No far-field flow is present. Flow lines are visualized in blue and non-dimensional time contours in red. Non-dimensional time spacing between contours: $t^* = 0.025$. (a) Impermeable fault with centre at the origin and angle $\beta = 135°$. (b) Leaky fracture added: 10 point sinks equally spaced from $-0.2 - 0.25i$ to $0.2 - 0.25i$, each with strength $m^* = -0.1$. (c) Second leaky fracture is added: 10 point sinks equally spaced from $0.05 + 0i$ to $0.45 + 0i$, each with strength $m^* = -0.1$.

(eq. 5), resulting in internal recirculation patterns (vortices) shaped as Cassinian ovals (Figs 16d and e).

Two mobile stagnation points develop, which are initially situated far away from the line doublet when the antipolar far-field flow rate is relatively weak with respect to the line doublet strength. However, these stagnation points move towards the line doublet when the relative strength of the far-field flow increases. Ultimately, any far-field flow that is strong enough will breach through the line doublet, which then splits into two vortices. Once touching the line doublet, each of the stagnation points is attracted by the two vortices, which is a new insight first documented in this study. At very high far-field flow rates the vortices vanish, and only two stagnation points remain. Fluid recirculation which was initially confined to two half-spaces separated by a single streamline of injection fluid instead becomes separated by a wide zone of penetrating far-field fluid from the aquifer. The vanishing of the vortices as far-field flow increases in strength (Fig. 16) is similar to the vanishing of the antipolar point doublet when far-field rate increases (Fig. 4).

Additionally, misalignment of the line doublet with respect to the far-field flow direction also causes a breakdown of the line doublet (Fig. 17). However, even if the line doublet breaks down it is still a direct-line-drive well-design and we have shown how it is no longer effectively doing what it was designed for. This conceptual insight is useful for, among others, management of groundwater flow, improved hydrocarbon recovery and geothermal well planning.

8.3 Flow across leaky fractures

We also visualized the flow of a direct line drive with and without the presence of an impermeable fault and leaky fractures (Figs 19 and 20). While an impermeable fault alone only shifts the streamlines from one producer to another and one leaky fracture only slightly changes the fluid flow, a significant change in the streamlines' pattern does appear when two leaky fractures occur, each at opposite sides of the fault, as they drain fluid from the reservoir. The two leaky fractures drain the majority of the visualized streamlines. Further simulations of streamline distortion and time of flight changes due to reservoir heterogeneities and anisotropy are discussed elsewhere (Weijermars *et al*. 2016; Weijermars & Zuo 2016).

In our study, we modelled flow across a high conductivity crack by a spaced point source and sink, which is identical to the flow effectuated by a first order line dipole as advocated by Strack (1989). Based on this observation, Appendix D shows that a first order line dipole mathematically is indeed the same flow as for a point source and sink pair.

8.4 Limitations and strengths of the method

We considered the practical implications and limitations of our analytical model for the systematic breakdown of a range of doublets. Multiple point sources, point sinks and singularity doublets can be included in any configuration desired. Additionally, instead of keeping well rates constant throughout the entire simulation, each element can be made time-dependent, and complex vector fields, pressure distribution, shear strain rates and principal strain rates can be visualized, as has been exemplified in an earlier study (Weijermars & Van Harmelen 2014). Structural features such as an impermeable fault can be incorporated into the reservoir, making

it possible to quickly visualize complex flow fields in a simple and elegant way. Our streamline model can trace injected fluid and time of flight contours. The accuracy of the streamlines is directly related to the non-dimensional time step Δt^* as well as the largest strength value of all the elements, m^*_{max}. A smaller value for Δt^* yields more accurate flow paths, but also increases computation time. A higher value for m^*_{max} requires a smaller Δt^* to maintain accurate stream lines. Computation time for flow visualization depends on (1) the number of particles traced, (2) the number of wells in the flow simulation and (3) the value of Δt^*.

When well rates vary over the life time of the doublet, the internal recirculation will be affected and can resemble shapes modelled elsewhere (Weijermars *et al.* 2014). For example, when the injection rates increase over time plume shapes will narrow downstream towards the producer (see fig. C2 in Weijermars *et al.* 2014). In contrast, when injection rates decrease over time plume shapes in such cases will widen faster then for the steady state Rankine shapes modelled in this study (as illustrated in fig. 18 of Weijermars *et al.* 2014).

8.5 Future work

Although thermal effects other than advective heat transport are not included in this study, conductive heat transfer can be readily incorporated in our model. Future work could build in conductive heat fluxes for specific geothermal well optimization studies. The heat content of the surfacing fluid will be determined by a combination of the conduction and advection of heat by the fluid in the reservoir as a result of its heat capacity, heat conductivity, ambient geothermal gradient, and the absolute rates of fluid injection and fluid extraction, accounting for the fluid admixture from any far-field flow and cooling in the shallow parts of the tubing, all of which depend on relative rates. The impact of the stated parameters on the thermal yield of the surfacing fluid is very sensitive to local conditions and cannot be sensibly scaled for any generic application. Each specific field application therefore requires dimensional scaling of heat transfer using the detailed inputs of all stated parameters for the particular case at hand. Such a specific application is not attempted in our this study, as our main focus is on the generic aspects of the flow recirculation as affected by the far-field flow.

9 CONCLUSIONS

The synthetic flow visualizations documented in our conceptual study may have significant practical value for real world geothermal and hydrocarbon well designs. The effects of any far-field flow on the confined recirculation of the injection fluid in a point doublet and a doublet composed of spaced wells can be significant. When the doublet symmetry plane is perfectly aligned with the far-field flow direction, all the injected fluid is contained in the space occupied by the cylinder (Figs 6a–d) or Rankine body (Figs 9a–d). Faster far-field flow-rates reduce the sweep region, but no far-field fluid enters the doublet recirculation. However, the closed-loop recirculation is lost when the baseline of the doublet becomes misaligned with respect to the far-field flow direction. For point doublets, the wells begin to entrain larger volumes of far-field fluid when the misalignment of the baseline between the injector and producer is at a larger angle with the far-field flow direction (Figs 7a–f). For doublets with spaced wells, misalignment of the doublet baseline with the far-field flow results in the production well producing larger fractions of far-field fluid. Additionally, more and more injection fluid will become

entrained by the far-field flow and travels downstream completely bypassing the producer well (Figs 10 and 11).

A line source or line sink can serve as a proxy for an array of point sources or sinks (Figs 12 and 14) on a macroscopic level. Therefore, instead of simulating flow from and to all point wells in a direct line drive, one can simulate a direct line drive by means of a single line source and line sink. The line doublet has practical applications in well planning for hydrocarbon and geothermal extraction, where spaced doublets in direct line drives are a commonly applied well design. The line doublet on a macroscopic level is an appropriate proxy for the spaced line source and line sink and therefore equally so for an array of spaced doublets (Figs 14 and 15). We have shown that a far-field flow may have a significant effect on the internal recirculation of any fluid injected into a reservoir by a line doublet. The possible breakdown of the line doublet due to the regional far-field may have negative effects on the drainage area and therefore a reduction in the efficiency of extraction of both geothermal energy and hydrocarbons may occur. While for antipolar orientation the injected fluid is contained within Cassinian ovals (Fig. 16), for a strong enough far-field flow the line doublet breaks into two segregated flow domains and as a consequence not all of the injected fluid will reach the producer side of the line doublet. Only for a relatively weak far-field flow, with respect to the line doublet's strength and length (eq. 5), does the line doublet's internal fluid recirculation not break apart. The far-field flow can in fact penetrate the line doublet for any alignment of the line doublet, as long as the former is strong enough. Moreover, in case of non antipolar alignment of the line doublet, a stronger far-field flow leads to less streamline jetting and less swirling in the neighborhood of the line doublet, and consequentially reduces the area of internal recirculation (Fig. 17a).

In addition to the breakdown of doublets by a far-field flow, we modelled the impact of reservoir heterogeneities, such as an impermeable fault and leaky fractures, on the doublet flow pattern. Such geological features may disrupt the planned doublet recirculation if not recognized timely during the planning of the well architecture and design. Recognition of such features based on closed-loop monitoring of pressure responses near the wells has been elaborated in a companion study (Weijermars *et al.* 2016). Application of our method in a specific field example is not attempted here. Such studies are typically in the realm of sponsored client studies requiring significant investment in data acquisition for reservoir characterization (Anderson *et al.* 2013) and dynamic reservoir modelling, with limited opportunity for release of proprietary results in the public domain. Based on the methods published here, our team is prepared to engage in such proprietary studies when the need arises. The conceptual insight offered by our studies may lead to improved well layout based on predrilling surveys of reservoir attributes and aquifer flow characteristics. Methods for geothermal energy harvesting can be applied, calibrated and improved to determine whether a project might be economically feasible (Griggs 2004; Erdlac *et al.* 2006; MIT 2006; Erdlac 2007; Blackwell *et al.* 2010; Jennejohn 2010; Airhart 2011; Booz/Allen/Hamilton 2014).

REFERENCES

Adams, C.A., Auld, A.M.C., Gluyas, J.G. & Hogg, S., 2015. Geothermal energy—the global opportunity, *Proc. Inst. Mech. Eng. Part A: J. Power Energy,* **229**(7), 747–754.

Airhart, M., 2011. A Second Look—Sizing Up the Potential for Geothermal Energy in Texas. Available at: http://www.beg.utexas.edu/pubs/pdf/a-second-look.pdf, last accessed 3 November 2011.

Anderson, A. *et al.*, 2013. National geothermal data system (NGDS) geothermal data domain: assessment of geothermal community data needs, in *Proceedings of the 38th Workshop on Geothermal Reservoir Engineering,* Stanford University, CA, February 11–13.

Barton, C.A., Hickman, S., Morin, R.H., Zoback, M.D., Finkbeiner, T., Sass, J. & Benoit, D., 1997. Fracture permeability and its relationship to in-situ stress in the Dixie Valley, Nevada, geothermal reservoir, in *Proceedings of the 22nd Workshop on Geothermal Reservoir Engineering,* Stanford University, pp. 147–152, January 27–29.

Batchelor, G.K., 1967. *An Introduction to Fluid Dynamics,* Cambridge Univ. Press.

Bellini, A., 2013. Cyclic and continuous flow systems: analytical and numerical models, *Ms. Eng. thesis,* Department of Industrial Engineering, University of Padova.

Bertani, G., Casinin, M., Gianelli, G. & Pandelli, E., 2006. Geological Structure of a long-living geothermal system, *Larderello, Italy. Terra Nova,* **18,** 163–169.

Bjarkason, E.K., 2014. Predicting thermal drawdown in geothermal systems using interwell tracer tests, Faculty of Earth Sciences, University of Iceland.

Bjornsson, A. & Hersir, G.P., 1981. Geophysical reconnaissance study of the Hengill high-temperature geothermal area, SW-Iceland, *Trans. Geotherm. Resour. Counc.,* **5,** 55–58.

Blackwell, D., Richards, M & Stepp, P., 2010. Final Report. Texas Geothermal Assessment for the I35 Corridor East, *Prepared for Texas State Energy Conservation Office. Contract CM709. March 29, 2010.* Southern Methodist University.

Booz/Allen/Hamilton, 2014. Market Trends Report 2013. Geothermal Technologies Office. DOE, Energy Efficiency & Renewable Energy. January 2014.

Brilleslyper, M.A., Dorff, M.A., McDougall, J.M., Rolf, J., Schaubroeck, L.E., Stankewitz, R.L. & Stephenson, K., 2012. *Explorations in Complex Analysis,* Mathematical Association of America Inc.

Browne, P.R.L., 1978. Hydrothermal alteration in active geothermal fields, *Ann. Rev. Earth planet. Sci.,* **6,** 229–250.

Da Costa, J.A. & Bennett, R.R., 1960. The pattern of flow in the vicinity of a recharging and discharging pair of wells in an aquifer having areal parallel flow, *Int. Ass. Sci. Hydrol. Publ.,* **52,** 524–536.

Dalton, C. & Helfinstine, R.A., 1971. Potential flow past a group of circular cylinders, *J. Basic Eng.,* **93**(04), 636–642.

Datta-Gupta, A. & King, M.K., 2007. *Streamline Simulation: Theory and Practice,* Textbook Series, SPE.

Doddema, L., 2012. The influence of reservoir heterogeneities on geothermal doublet performance, Training report, Master Programme Energy and Environmental Sciences, University of Groningen.

Drange, L.A., 2011. Engineered geothermal systems, Master of Science in Product Design and Manufacturing. Department of Energy and Process Engineering, Norwegian University of Science and Technology.

Erdlac, R.J., 2007. Geopowering Texas. A report to the Texas state energy conservation office on developing the geothermal energy resource of Texas, January 2007.

Erdlac, R.J., Jr., Armour, L. & Lee, R., 2006, A Resource Assessment of Geothermal Energy Resources for Converting Deep Gas Wells in Carbonate Strata into Geothermal Extraction Wells: A Permian Basin Evaluation: Department of Energy, National Renewable Energy Laboratory, Golden, CO., Contract No. DE-FG36-05GO-85023.

Faulds, J.E., Hinz, N. & Kreemer, C., 2012. Structural and tectonic controls of geothermal activity in the Basin and Range province, Western US, in Proceedings of New Zealand Geothermal Workshop, Auckland, New Zealand, 2012 November 19–21.

Ferrill, D.A. & Morris, A.P., 2003. Dilational normal faults, *J. Struct. Geol.,* **25,** 183–196.

Fossen, H., 2010. *Structural Geology,* Cambridge Univ. Press.

Giacchetta, G., Leporini, M. & Marchetti, B., 2015. Economic and environmental analysis of a Steam Assisted Gravity Drainage (SAGD) facility for oil recovery from Canadian oil sands, *Appl. Energy,* **142,** 1–9.

Griggs, J., 2004. A re-evaluation of geopressured-geothermal aquifers as an energy resource, *MS thesis,* Lousiana State University. August 2004.

Hecht Mendez, J., 2012. Optimization of shallow closed-loop geothermal systems, *PhD thesis,* Mathematisch-Naturwissenschaftlichen Fakultät der Eberhard Karls Universität Tübingen.

Hickman, R.G., Dobson, P.F., van Gerven, M., Sagala, B.D. & Gunderson, R.P., 2004. Tectonics and stratigraphic evolution of the Sarulla graben geothermal area, North Sumatra, Indonesia, *J. Asian Earth Sci.,* **23**(3), 435–448.

Hirst, C.M., Gluyas, J.G. & Mathias, S.A., 2015. The late field life of the East Midlands Petroleum Province; a new geothermal prospect, *Q. J. Eng. Geol. Hydroge.,* **48,** 104–114.

Holzbecher, E., 2005. Analytical solution for two-dimensional groundwater flow in presence of two isopotential lines, *Water Resour. Res.,* **41**(12), 1–7.

Holzbecher, E. & Sauter, M., 2010. The doublet system simulator, in *Proceedings of the World Geothermal Congress 2010,* Bali, Indonesia, 2010 April 25–29 April.

Holzbecher, E., Oberdorfer, P., Maier, F., Jin, Y. & Sauter, M., 2011. Simulation of deep geothermal heat production, in *Proceedings of the 2011 COMSOL Conference 2011,* Stuttgart, Germany, 26–28 October.

Houwers, M.E., Heijnen, L.J., Becker, A. & Rijkers, R., 2015. A workflow for the estimation of fault zone permeability for geothermal production: A general model applied on the ROER Valley Graben in the Netherlands, in *Proceedings of the World Geothermal Congress*, Melbourne, Australia, 2015 April 19–25.

Jelgersma, F., 2007. Redevelopment of the abandoned Dutch onshore Schoonebeek oilfield with gravity assisted steam flooding, in *Proceedings of the International Petroleum Technology Conference 2007,* Dubai, United Arabic Emirates, 2007 December 4–6. doi:10.2523/11700-MS

Jennejohn, D., 2010. *US Geothermal Power Production and Development Update,* Geothermal Energy Association.

Kuethe, A.M. & Chow, C.Y., 1998. *Foundations of Aerodynamics—Bases of Aerodynamics Design,* 5th edn, pp. 96–102, John Wiley & Sons, Inc.

Lund, J., Sanner, B., Rybach, L., Curtis, R. & Hellström, G., 2004. Geothermal (ground-source) heat pumps a world overview, *Geo-Heat Centre Quart. Bull. (September 2004),* **25**(3), 1–10.

Milne-Thomson, L.M., 1962. *Theoretical Hydrodynamics,* 4th edn, pp. 200–208, Macmillan and Co. Ltd.

MIT, 2006. The Future of Geothermal Energy. Impact of Enhanced Geothermal Energy Systems (EGS) on the United States in the 21st Century, An assessment by an MIT-led interdisciplinary panel. Available at: http://mitei.mit.edu/publications/reports-studies/future-geothermal-energy.

Nukman, M. & Moeck, I., 2013. Structural controls on a geothermal system in the Tarutung Basin, north central Sumatra, *J. Asian Earth Sci.,* **74,** 86–96.

Omenda, P. & Teklemariam, M., 2010. Overview of geothermal resource utilization in the east African rift system, *Presented at Short Course V on Exploration for Geothermal Resources,* Lake Bogoria and Lake Naivasha, Kenya, 2010 October 29–November 19.

Onacha, S., Shalev, E., Malin, P., Leary, P. & Bookman, L., 2010. Interpreted fracture anomalies: joint imaging of geophysical signals from fluid-filled fracture zones in geothermal fields, in *Proceedings of the World Geothermal Congress,* Bali, Indonesia, April 25–29.

Potter, H.D.P., 2008. On conformal mappings and vector fields, *Senior thesis,* Marietta College, Marietta, Ohio.

Røgen, B., Ditlefsen, C., Vangkilde-Pedersen, T., Nielsen, L.H. & Mahler, A., 2015. Geothermal energy use, 2015 country update for Denmark, in *Proceedings of the World Geothermal Congress 2015,* Melbourne, Australia, 2015 April 19–25.

Rosenberg, M.D., Bignall, G. & Rae, A.J., 2009. The geological framework of the Wairakei–Tauhara geothermal system, New Zealand, *Geothermics,* **38**(1), 72–84.

Rowlands, J.V. & Sibson, R.H., 2004 Structural controls on hydrothermal flow in a segmented rift system, Taupo Volcanic Zone, New Zealand, *Geofluids,* **4**(4), 259–283.

Soldo, E. & Alimonti, E., 2015. From an oilfield to a geothermal one—use of a selection matrix to choose between two, in *Proceedings of the World Geothermal Congress 2015,* Melbourne, Australia, 2015 April 19–25.

Strack, O.D.L., 1989. *Groundwater Mechanics,* Prentice Hall.

Tomaszewska, B. & Pajak, L., 2012. Dynamics of clogging processes in injection wells used to pump highly mineralized thermal waters into the sandstone structures lying under the polish lowlands, *Arch. Environ. Protect.,* **38**(3), 105–117.

Twiss, R.J. & Moores, E.M., 2000. *Structural Geology,* 6th edn, W.H. Freeman & Co.

Weijermars, R., 1993. Estimation of palaeostress orientation within deformation zone between two mobile plates, *Geol. Soc. Am. Bull.,* **105,** 1491–1510.

Weijermars, R., 1998. *Principles of Rock Mechanics,* 2nd edn, Alboran Science Publishing.

Weijermars, R., 2014. Visualization of space competition and plume formation with complex potentials for multiple source flows: some examples and novel application to Chao lava flow (Chile), *J. geophys. Res.: Solid Earth,* **113**(3), 2397–2414.

Weijermars, R., 2015. Salt sheet coalescence in the Walker Ridge region (Gulf of Mexico): insights from analytical models, *Tectonophysics,* **640–641,** 39–52.

Weijermars, R. & Poliakov, A., 1993. Stream functions and complex potentials: implications for development of rock fabric and the continuum assumption, *Tectonophysics,* **220,** 33–50.

Weijermars, R. & Schmeling, H., 1986. Scaling of Newtonian and non-Newtonian fluid dynamics without inertia for quantitative modelling of rock flow due to gravity (including the concept of rheological similarity), *Phys. Earth planet. Inter.,* **43**(4), 316–330.

Weijermars, R. & Van Harmelen, A., 2014. Quantifying velocity, strain rate and stress distribution in coalescing salt sheets for safer drilling, *Geophys. J. Int.,* **200,** 1483–1502.

Weijermars, R. & Zuo, L., 2016. Time of flight and flight path controls of fluid flow in heterogeneous isotropic and anisotropic porous media: new evidence from streamline simulations, *J. Fluid Mech.,* in press.

Weijermars, R., Dooley, T.P., Jackson, M.P.A. & Hudec, M.R., 2014. Rankine models for time-dependent gravity spreading of terrestrial source flows over subplanar slopes, *J. geophys. Res.: Solid Earth,* **120**(6), 4616–4644.

Weijermars, R., Van Harmelen, A. & Zuo, L., 2016. Controlling flood displacement fronts using a parallel analytical streamline simulator, *J. Petr. Sci. Eng.,* **139,** 23–42.

White, F.M., 2011. *Fluid Mechanics,* 7th edn, McGraw Hill.

SUPPORTING INFORMATION

Additional Supporting Information may be found in the online version of this paper:

Two animations based on time series of Figures 19 and 20 are available online as supplementary information. (http://gji.oxfordjournals.org/lookup/suppl/doi:10.1093/gji/ggw135/-/DC1).

Please note: Oxford University Press is not responsible for the content or functionality of any supporting materials supplied by the authors. Any queries (other than missing material) should be directed to the corresponding author for the paper.

APPENDIX A: ANALYTICAL ELEMENTS

A1 Terminology for singularity doublets, spaced doublets, line doublets and dipoles

Throughout this study we have used a mixture of terms like source, sink, injector, producer, point, line, doublet, dipole, singularity, linear array and spaced. This section serves as a clarification of these terms by explaining and visualizing them and all their mixtures (Fig. A1).

With the terms source and injector we mean the same: an analytical element that adds fluid to the reservoir and is denoted by a plus sign (Fig. A1, Row 1, Column a). The terms sink and producer refer to an analytical element that removes fluid from the reservoir and is denoted by a minus sign (Fig. A1, Row 2, Column a).

The term 'point' refers to an analytical element that exists as a single point in the reservoir. A point source (sink) is therefore an analytical element that adds (removes) fluid to (from) the reservoir and is located in a single coordinate (Fig. A1 Rows 1 and 2, Column a).

Multiple point sources (sinks) are also called a linear array of point sources (sinks, Fig. A1, Rows 1 and 2, Column b). The term 'line' on the other hand describes an analytical element which exists as a straight line between two coordinates that contains infinitely many points. A line source adds fluid to the reservoir (Fig. A1, Row 1, Column c), while a line sink drains the reservoir (Fig. A1, Row 2, Column c). Whenever there is a source/sink pair with space between them, the term 'spaced' is added (Fig. A1, Rows 1–3, Columns a–c).

A point doublet, or singularity doublet, is an analytical element where one side of the singularity is the injector side and the other side is the producer side (Fig. A1, Row 4, Column a). Analogous to the line source (sink), a line doublet refers to an analytical element which exists as a straight line between two coordinates that contains infinitely many singularity doublets (Fig. A1, Row 4, Column c). The distinction between a singularity doublet and singularity dipole becomes important when considering a linear array of singularity doublets (Fig. A1, Row 4, Column b) or of singularity dipoles (Fig. A1, Row 5, Column b) as their flow regimes will be different (Strack 1989). The point (or singularity) dipole is an analytical element similar to the singularity doublet, but the injector and producer sides are rotated 90° clockwise (Fig. A1, Row 5, Column a). A line dipole contains infinitely many singularity dipoles (Fig. A1, Row 5, Column c).

A2 Flow through a high conductivity crack: the line dipole

Strack (1989) distinguished between line dipoles and line doublets. A line dipole is made up of a series of closely spaced alternating injector and producer poles oriented, in contrast to the line doublet (see also Appendix A1), along the trend of the line interval (Fig. A2a). This line dipole is an analytical element suitable for modelling flow through discrete fractures of high conductivity. The 90° change in orientation of
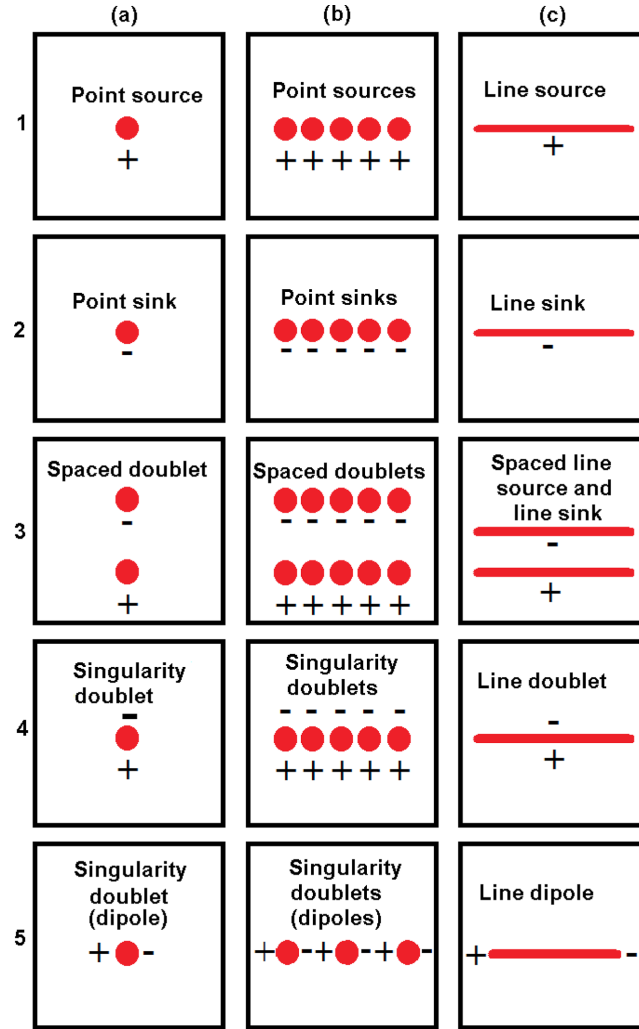
Figure A1. Visualization of analytical elements and use of doublet terms and line dipole referred to in our study.

the injector and producer poles, as compared to the line doublet, results in discrete jumps of the stream function ψ while the equipotential ϕ remains continuous (Strack 1989).

Figs A2(a)–(c) summarizes various simulations of a line dipole using first-order line integrals, with the strengths of injector and producer poles distributed uniformly over the length of the line dipole. The supporting equations are detailed in Appendix D. Initially, no far-field was superposed. Fig. 8(a) used a series of point dipoles (see for terminology Appendix A1) with similar strengths, and evenly spaced along the interval of the line dipole. Fig. A2(b) used a uniform strength distribution along the interval of the line dipole. Fig. A2(c) used a discrete pair of a sink and source spaced by the same interval as the line dipole. It appears that the results of Figs. A2(b) and A2(c) are indistinguishable. This leads us to conclude that a line dipole with a uniform strength distribution as defined by Strack (1989) is identical to a sink and source pair spaced by the same interval as the line dipole, which we subsequently prove mathematically in Appendix D.

Superposing a far-field flow on the line dipole does effectuate steep accelerations of the flow in the vicinity of the paired source and sink, but no abrupt jumps in ψ occur (Fig. A3a). The steep gradient of ψ of the first-order line dipole can be compressed into a more abrupt higher-order line dipole for representing the conductive crack. Fig. A3(b) shows Strack's (1989) portrayal of a line dipole acting as a high conductivity crack for a far-field flow and appears virtually identical to our flow simulation of Fig. A3(a), which used a source/sink pair to simulate the flow through a high conductivity crack.

APPENDIX B: DESCRIPTION OF SINGULARITY DOUBLET IN FAR-FIELD FLOW AND DERIVATION OF STAGNATION POINTS

B1 Singularity doublet in far-field flow construction

A point source, located at the complex coordinate z_d with strength m^*, can be modelled through the use of complex potentials. The complex vector field, defined as the derivative of the complex potential, for a point source is given by (Brilleslyper *et al.* 2012)

$$V(z) = \frac{m^*}{z - z_d}. \tag{B1}$$
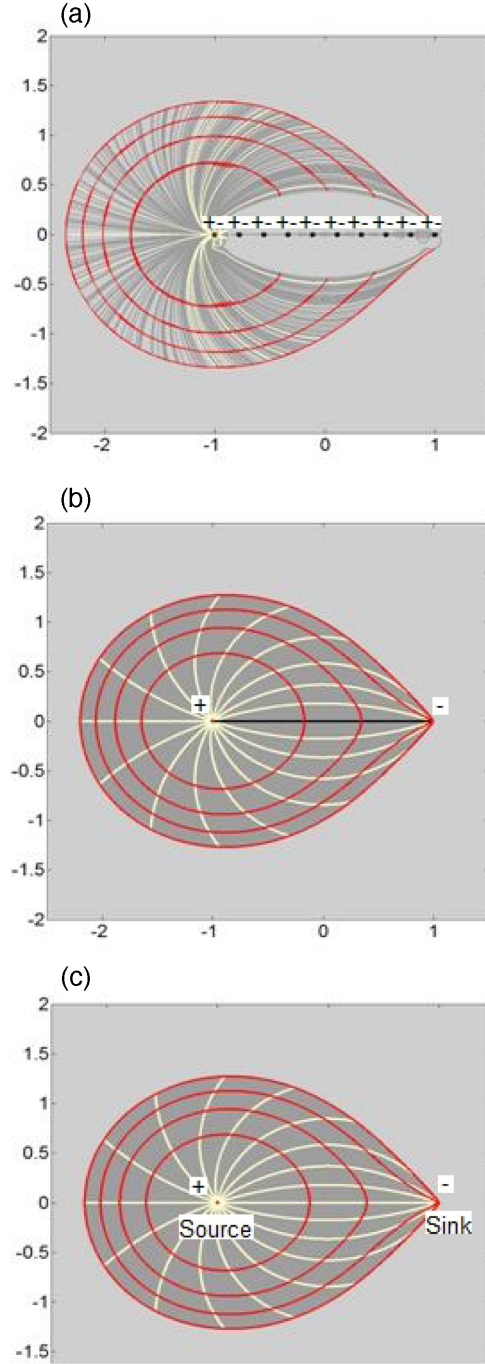
Figure A2. Line dipole simulations using various approaches. No far-field present. (a) streamlines for a line dipole approximation using a string of singularity doublets with weighed strengths approximately equal to the total strength of case b. (b) Continuous solution of true line dipole of length 2 and strength $m^* = 1$. (c) Point source and sink of strength $m^* = 0.5$ and $m^* = -0.5$ separated by distance 2, equal to the line dipole length of case b, yielding identical result as compared to case b (see also Appendices D1 and D2).

The complex vector field for a spaced doublet is obtained combining the expressions for a point source and a point sink, respectively located at z_1 and z_2 with strengths m^* and $-m^*$ (Weijermars 2014; Weijermars *et al.* 2016):

$$V(z) = \frac{m^*}{z - z_1} - \frac{m^*}{z - z_2}$$

$$= \frac{m^*(z_1 - z_2)}{(z - z_1)(z - z_2)}. \tag{B2}$$

The singularity doublet, or point doublet, can be obtained using a limiting process that decreases the distance between the point source and point sink. Let the point source and point sink of equal strengths therefore be located at a distance ε from the origin, respectively at $z = -\varepsilon$
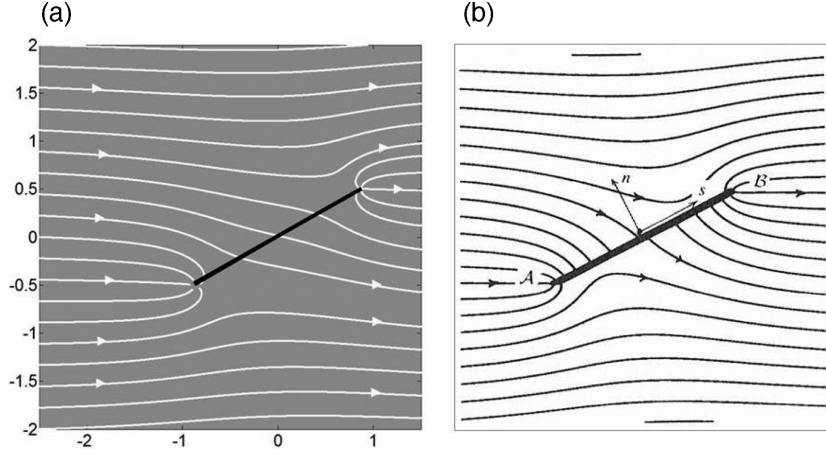
Figure A3. (a) First-order line dipole with total strength of line dipole $m^* = 1$, equivalent to a sink and source pair of strength $m^* = 0.5$ and $m^* = -0.5$ separated by non-dimensional distance 2, oriented at angle $210°$. Far-field flow strength $U_y^* = 2$ and angle $0°$. **(b)** Streamlines for highly conductive crack diverting a far-field flow, according to Strack (1989).

and $z = \varepsilon$, with ε a real number. The distance between the point source and sink is equal to 2ε. By letting $\varepsilon \to 0$ the point source and sink come close in on each other. The point doublet is obtained once both are located at the origin.

However, keeping their strengths constant regardless of the distance between the point source and -sink, would render the complex vector field zero when $\varepsilon = 0$:

$$V(z) = \lim_{\varepsilon \to 0} \frac{m^*}{z + \varepsilon} - \frac{m^*}{z - \varepsilon}$$

$$= \lim_{\varepsilon \to 0} \frac{-2\varepsilon \cdot m^*}{(z + \varepsilon)(z - \varepsilon)} = 0. \tag{B3}$$

In order to prevent $V(z) = 0$ for $\varepsilon = 0$, the respective strengths of the point source and sink are increased inversely proportional to the distance between them. This way, when the distance is for example halved, the strength is doubled, thus preventing $V(z) = 0$ for $\varepsilon = 0$. The distance between the source and sink is equal to 2ε, which requires multiplying the strength in the numerator of eq. (B3) by $1/2\varepsilon$. The resulting complex vector field is:

$$V(z) = \lim_{\varepsilon \to 0} \frac{m^*}{2\varepsilon} \frac{1}{z + \varepsilon} - \frac{m^*}{2\varepsilon} \frac{1}{z - \varepsilon}$$

$$= \lim_{\varepsilon \to 0} \frac{m^*}{2\varepsilon} \frac{-2\varepsilon}{(z + \varepsilon)(z - \varepsilon)}$$

$$= \frac{-m^*}{z^2}. \tag{B4}$$

The orientation of the singularity doublet described by eq. (B4) is shown in Fig. 1. Rotating the singularity of eq. (B4) counter-clockwise by an angle β is achieved using the conformal mapping $f(z) = z \cdot e^{-\beta i}$. This yields the complex vector field:

$$V[f(z)] \cdot f'(z) = \frac{-m^*}{(ze^{-\beta i})^2} \cdot e^{-\beta i} = \frac{-m^* \cdot e^{\beta i}}{z^2}. \tag{B5}$$

Allocating the doublet to any location $z_d = x_d + i y_d$ requires the mapping $f(z) = z - z_d$, yielding the singularity doublet vector field expression:

$$V(z) = \frac{-m^* \cdot e^{\beta i}}{(z - z_d)^2}. \tag{B6}$$

Superposing a far-field flow with strength U_x^* flowing at an angle α with respect to the x-axis results in the vector field:

$$V(z) = U_x^* e^{-\alpha i} + \frac{-m^* \cdot e^{\beta i}}{(z - z_d)^2}. \tag{B7}$$

B2 Derivation of the stagnation points for singularity doublet with far-field flow

The location of the stagnation points for the vector field of eq. (B7) are obtained by solving $V(z) = 0$, that is:

$$U_x^* e^{-\alpha i} + \frac{-m^* \cdot e^{\beta i}}{(z - z_d)^2} = 0. \tag{B8}$$

The complex valued solution of eq. (B8) is then given by

$$(z - z_d) = \pm \sqrt{\frac{m^*}{U_x^*}} \cdot e^{\frac{(\beta + \alpha)i}{2}}. \tag{B9}$$

Expression (B9) yields in Cartesian coordinates the stagnation points (x_{sp}, y_{sp}):

$$\begin{cases} x_{sp} = x_d \pm \sqrt{\frac{m^*}{U_x^*}} \cos\left(\frac{\beta + \alpha}{2}\right) \\ y_{sp} = y_d \pm \sqrt{\frac{m^*}{U_x^*}} \sin\left(\frac{\beta + \alpha}{2}\right) \end{cases}. \tag{B10}$$

B3 Derivation of the stagnation points for Rankine body with far-field flow

Superposing far-field flow with velocity U_x^* and angle α onto the vector field for a point source and point sink with, respectively strengths m^*_1 and m^*_2, yields the following vector field:

$$V(z) = U_x^* e^{-\alpha i} + \frac{m^*_1}{z - z_1} + \frac{m^*_2}{z - z_2}. \tag{B11}$$

Finding the stagnation points amounts to solving again the equation $V(z) = 0$. Eq. (B11) is first rewritten into a quadratic equation:

$$0 = z^2 - \left[z_1 + z_2 - \frac{(m^*_1 + m^*_2)}{U_x^* e^{-\alpha i}} \right] z + z_1 z_2 - \frac{m^*_1 z_2 + m^*_2 z_1}{U_x^* e^{-\alpha i}}, \tag{B12}$$

after which the following solution gives the complex coordinates for the stagnation points z_{sp}:

$$z_{sp} = \frac{z_1 + z_2 - \frac{(m^*_1 + m^*_2)}{U_x^* e^{-\alpha i}} \pm \sqrt{\left(z_1 + z_2 - \frac{(m^*_1 + m^*_2)}{U_x^* e^{-\alpha i}} \right)^2 - 4 \cdot \left(z_1 z_2 - \frac{m^*_1 z_2 + m^*_2 z_1}{U_x^* e^{-\alpha i}} \right)}}{2}. \tag{B13}$$

Simplifying (B13) results in the expression for the stagnation points (in complex coordinates):

$$z_{sp} = \frac{z_1 + z_2 - \frac{m^*_1 + m^*_2}{U_x^* e^{-\alpha i}} \pm \sqrt{\left(z_1 - z_2 - \frac{m^*_1 - m^*_2}{U_x^* e^{-\alpha i}} \right)^2 + \frac{4 m^*_1 m^*_2}{\left(U_x^* e^{-\alpha i} \right)^2}}}{2}. \tag{B14}$$

APPENDIX C: LINE SOURCE/SINK AND LINE DOUBLET

C1 Derivation of the complex vector field of a line source/sink

In this section we derive the complex vector field of a line source (m^* positive); a line sink is described by the same function (m^* negative).

The vector field for n point sources of combined strength m^*, located at the real x-coordinates x_k is (Potter 2008):

$$V(z) = \sum_{k=1}^{n} \frac{1}{n} \frac{m^*}{z - x_k}. \tag{C1}$$

In order to transform eq. (C1) into a Riemann integral, we assume that the n point sources are spaced evenly inside the real interval [a, b]. By defining the distance between two neighbouring point sources as

$\Delta x_k = x_{k+1} - x_k = (b - a)/n$, eq. (C1) becomes (Potter 2008):

$$V(z) = \sum_{k=1}^{n-1} \frac{\Delta x_k}{b - a} \frac{m^*}{z - x_k} + \frac{1}{n} \frac{m^*}{z - x_n}. \tag{C2}$$

For $n \to \infty$ the last term in eq. (C2) vanishes and the desired Riemann integral is obtained as the spacing Δx_k goes to zero, which yields the vector field for a horizontal line source:

$$V(z) = \frac{m^*}{b - a} \int_a^b \frac{1}{z - x_k} \mathrm{d}x_k$$

$$= \frac{m^*}{b - a} \left[\log(z - a) - \log(z - b) \right]. \tag{C3}$$

Rotating the line source of eq. (C3) counter-clockwise by β radians is achieved by evaluating $V[f(z)] \cdot f'(z)$ for the conformal mapping $f(z) = e^{-i\beta} z$. The endpoints of the line source after rotation are the complex coordinates z_a and z_b. After simplification, the rotation of eq. (C3) results in a general expression for the vector field of a line source of length $b - a$, centred at $(z_a + z_b)/2$ and with angle β:

$$V(z) = \frac{m^*}{b - a} \left[\log(z - z_a) - \log(z - z_b) \right] e^{-i\beta} \tag{C4}$$

with $m^* < 0$ for a line sink and $m^* > 0$ for a line source.

C2 Derivation of the complex vector field of a line doublet

There are two approaches to derive the vector field for the line doublet (Fig. 5c). The first one entails collapsing the distance between a spaced line source and line sink (Figs 14 and 15). The second approach combines many singularity doublets to derive the complex vector field equation for a line doublet. We illustrate the latter approach in this section, starting from the singularity doublet (Fig. 5a) which is the collapsed version of the spaced doublet (Fig. 5b). The mathematical derivation of the vector field for a singularity doublet based on a point source and point sink can be found in Appendix B1. For a single singularity doublet located at the x-coordinate x_k, with strength m^* and with orientation as in Fig. 5(a), the vector field reads:

$$V(z) = \frac{-im^*}{(z - x_k)^2}. \tag{C5}$$

The complex vector field for n singularity doublets located on the real axis, with total uniform strength m^*, is:

$$V(z) = \sum_{k=1}^{n} \frac{1}{n} \frac{-im^*}{(z - x_k)^2}. \tag{C6}$$

In order to transform eq. (C6) into a Riemann integral, analogous to the derivation of a line source in Section C1, assume that the n singularity doublets are spaced evenly inside the real interval [a,b]. By defining the distance between two neighbouring singularity doublets as $\Delta x_k = x_{k+1} - x_k = (b - a)/n$, the above formula becomes:

$$V(z) = \sum_{k=1}^{n-1} \frac{\Delta x_k}{b - a} \frac{-im^*}{(z - x_k)^2} + \frac{1}{n} \frac{-im^*}{(z - x_n)^2}. \tag{C7}$$

For $n \to \infty$ the last term in eq. (C7) vanishes and a valid Riemann integral is obtained as the spacing Δx_k goes to zero, which yields the vector field for a horizontal line doublet:

$$V(z) = \frac{-im^*}{b - a} \int_a^b \frac{1}{(z - x_k)^2} \, dx_k$$

$$= \frac{-im^*}{(z - b)(z - a)}. \tag{C8}$$

Rotating the line doublet counter-clockwise by β radians is achieved by evaluating $V[f(z)] \cdot f'(z)$ for the conformal mapping $f(z) = e^{-i\beta} z$; the general velocity field expression for a line doublet of uniform strength (where z_a and z_b are the complex coordinates after rotation) is:

$$V(z) = \frac{-im^*}{(z - z_b)(z - z_a)} e^{i\beta}. \tag{C9}$$

C3 Superposition of far-field flow and a line doublet: stagnation points

Locating the stagnation points for a flow regime containing a line doublet and a far-field flow of strength $U_y{}^*$ and angle α, comes down to solving $V(z) = 0$ for the corresponding vector field (Figs 16 and 17):

$$V(z) = U_y{}^* e^{-\alpha i} + \frac{-im^*}{(z - z_b)(z - z_a)} e^{\beta i}. \tag{C10}$$

Setting expression (C10) equal to zero, the resulting equation is rewritten into a quadratic equation:

$$z^2 - (z_a + z_b)z + z_a z_b - \frac{im^*}{U_y{}^*} e^{(\alpha + \beta)i} = 0. \tag{C11}$$

Solving this quadratic equation reveals the location of the stagnation points z_{sp}:

$$z_{sp} = \frac{z_a + z_b \pm \sqrt{(z_a - z_b)^2 + 4 \frac{im^*}{U_y{}^*} e^{(\alpha + \beta)i}}}{2}. \tag{C12}$$

C4 Special stagnation point: occurrence of a lemniscate

The stagnation point that corresponds with the formation of a lemniscate is located in the midpoint of the line doublet, that is at $z_{sp} = (z_a + z_b)/2$. The lemniscate occurs only for antipolar alignment, that is for a line doublet with orthogonal orientation with respect to the far-field orientation. Such an orientation is shown in Fig. 16(c), with far-field angle $\alpha = 90°$ ($\pi/2$ radians) and line doublet angle $\beta = 0°$ (0 radians).

Substituting $z_{sp} = (z_a + z_b)/2$ and both angles in, respectively the left-hand side and right-hand side of eq. (C12), the lemniscate occurs if the following holds:

$$(z_a - z_b)^2 = 4 \cdot m^*/U_y{}^*. \tag{C13}$$

Due to the chosen angles, $(z_a - z_b)^2$ is the square of the length of the line doublet. Therefore a lemniscate develops when the ratio of the strength of the line doublet and far-field flow equals a quarter of the line doublet's length squared.

APPENDIX D: FLOW ACROSS LEAKY FRACTURES

It not only appears that the flow regime in Figs A2(b) and A2(c) are identical, one can mathematically prove this. The complex velocity field for a line dipole can be derived following steps similar to those of Appendix B2.

D1 Line dipole complex vector field

Rotating the singularity doublet (Fig. 1) 180° clockwise, the complex vector field of such a singularity doublet with strength m^*, located at the complex coordinate z_k, is given by:

$$V(z) = \frac{-m^*}{(z - z_k)^2}. \tag{D1}$$

The injector side (+) of the singularity doublet now points to the left and the producer side (–) now points to the right-hand side, instead of, respectively right- and left-hand sides as in Fig. 1. Going through the calculations of eqs (B6–B9), with eq. (D1) as a starting point, leads to the following formula for a line dipole:

$$V(z) = \frac{-m^*}{(z - z_b)(z - z_a)} e^{i\beta}. \tag{D2}$$

D2 Line dipole vector field from a point source/sink pair

The complex velocity field of a line dipole can also be obtained from a source/sink pair. For a single point source of strength m^* located at $z = z_a$, the field is given by

$$V(z) = \frac{m^*}{z - z_a}. \tag{D3}$$

The complex vector field for a point source and a point sink of equal strength, where the sink is located at $z = z_b$, is:

$$
\begin{aligned}
V(z) &= \frac{m^*}{z - z_a} - \frac{m^*}{z - z_b} \\
&= \frac{-m^*}{(z - z_a)(z - z_b)} \cdot (z_b - z_a) \\
&= \frac{-m^* \cdot (b - a)}{(z - z_a)(z - z_b)} \cdot e^{i\beta}.
\end{aligned} \tag{D4}
$$

Comparing eqs (D4) and (D2), we find that the vector fields become equal if the strength of eq. (D2) is scaled as $m^*(b-a)$. In Fig. A2(c) the strength of the source/sink pair is scaled such that $m^*(b-a)$ equals the strength of the line dipole (Fig. A2b).

APPENDIX E: COMPLEX VECTOR FIELD EQUATION FOR AN IMPERMEABLE FAULT

Through conformal mapping we transform the complex potential plane to include one of a variety of impermeable boundaries. In this study we showcased an impermeable fault and in this Section we explain how the complex potential and the complex vector field for flow around such a fault are obtained. We consider an impermeable fault at the arbitrary location z_{if} in the reservoir, with arbitrary angle β and length $2a$.

E1 Far-field flow around an impermeable fault

Fig. E1(a) shows the impermeable fault first conveniently located in the origin, subject to a far-field flow rate U^* arriving at angle α. In order to derive the complex vector field that describes such a flow regime (Fig. E1a), conformal mapping is used to transform this flow regime into a flow regime for which the complex potential is already known (Fig. E1e). A flow regime for which the complex potential is known, is that of a uniform far-field flow (Fig. E1e). The complex potential of a uniform far-field flow can be used, because an infinitely thin impermeable fault oriented parallel to the flow direction does not affect the flow regime. The complex potential for a uniform far-field flow is:

$$\Omega(z) = U^* \cdot z. \tag{E1}$$

The first conformal mapping used, $k(z)$, rotates the entire flow field (Fig. E1a) into a flow regime where the fault's angle is brought back to 0 radians (Fig. E1b). This is achieved through the use of the mapping $k(z) = e^{-i\beta} \cdot z$. Consequentially, the far-field angle is now $\alpha - \beta$ and, in the end, this angle also must be reduced to zero as depicted in Fig. E1(e).
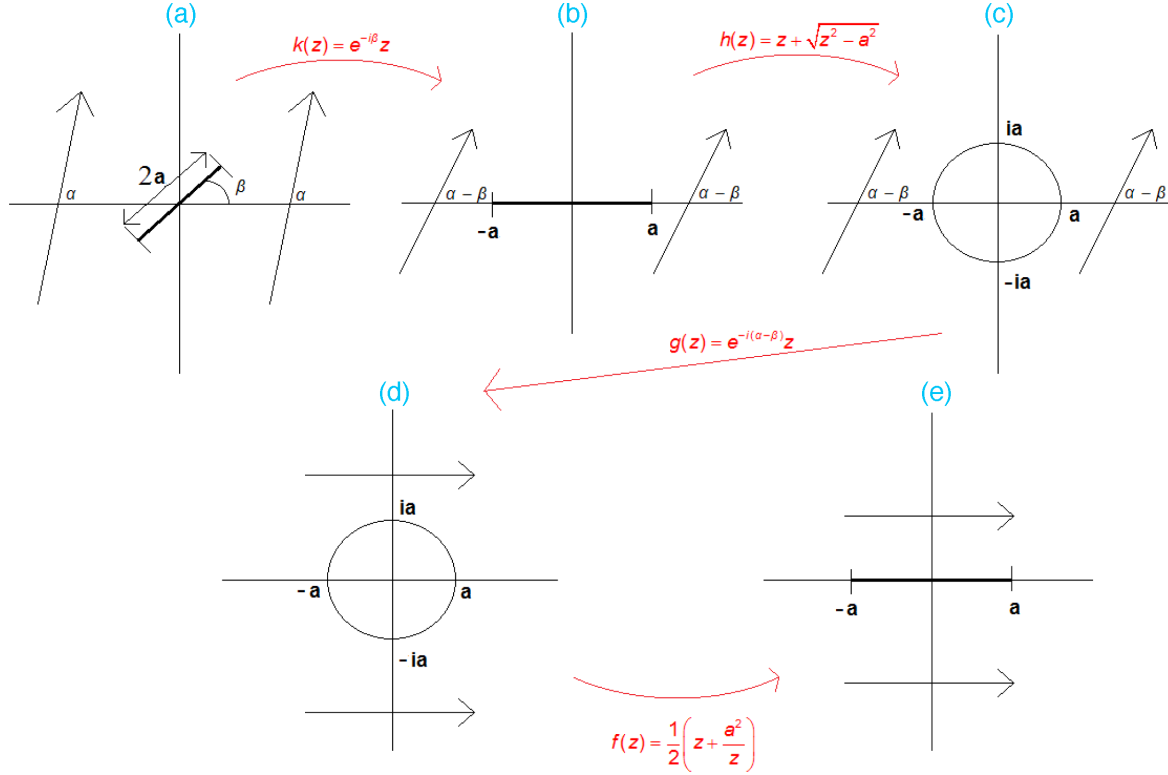
Figure E1. Visualization of conformal mapping operations used to derive complex potential for far-field flow past an impermeable fault.

Rotating the flow regime of Fig. E1(b) will unfortunately also rotate the fault and this is not desired. However, if the fault can be temporarily transformed into a circle, then the flow-field can be rotated to reduce the far-field angle to zero while the circle is left unchanged (Figs E1c and d). The conformal mapping that maps Fig. E1(b) into Fig. E1(c) is denoted by $h(z)$:

$$h(z) = z + \sqrt{z^2 - a^2}. \tag{E2}$$

Now that Fig. E1(a) has been mapped to Fig. E1(c), the next step is rotating the flow regime such that the far-field flow angle is zero (Fig. E1d). This is achieved by using the mapping $g(z) = e^{-i(\alpha-\beta)} \cdot z$.

The last conformal mapping transforms the flow-field (Fig. E1d) into the flow regime of a uniform far-field flow (Fig. E1e). This is accomplished through use of the following conformal mapping:

$$f(z) = \frac{1}{2} \left(z + \frac{a^2}{z} \right). \tag{E3}$$

Since all required conformal mapping is now known, we can derive the complex potential and subsequently the associated velocity field for far-field flow around an impermeable fault of arbitrary length and orientation. The complex potential is given by:

$$\tilde{\Omega}(z) = \Omega \left[k(h(g(f(z)))) \right]. \tag{E4}$$

Combining the complex potential (eq. E1) and all of the conformal mapping operations with eq. (E4), yields after some simplifications the complex potential:

$$\tilde{\Omega}(z) = U^* \cdot \frac{1}{2} e^{-i\beta} \left(e^{-i(\alpha-\beta)} \left(z + \sqrt{z^2 - (e^{i\beta}a)^2} \right) + e^{i(\alpha-\beta)} \left(z - \sqrt{z^2 - (e^{i\beta}a)^2} \right) \right). \tag{E5}$$

Differentiating this complex potential with respect to z, gives us the velocity field for far-field flow around an impermeable fault of length $2a$ with angle β:

$$V(z) = U^* \cdot e^{-i\beta} \left(\cos(\alpha - \beta) - i \sin(\alpha - \beta) \frac{z}{\sqrt{z^2 - (e^{i\beta}a)^2}} \right). \tag{E6}$$

The centre of the fault is still located at the origin, but this is easily remedied. Substitution of z by $z - z_{if}$ in expression (E6) shifts the centre of the fault to the complex coordinate z_{if}:

$$V(z) = U^* \cdot e^{-i\beta} \left(\cos(\alpha - \beta) - i \sin(\alpha - \beta) \frac{z - z_{if}}{\sqrt{(z - z_{if})^2 - (e^{i\beta}a)^2}} \right). \tag{E7}$$

E2 Point source/sink flow around an impermeable fault

The vector field of a point source or sink flow around an impermeable fault can be obtained following steps nearly identical to those of Section E1. The first two steps remain the same: first a rotation, via $k(z)$, is employed to align the fault with the x-axis, after which the mapping $h(z)$ transforms the fault into a circle. Consequentially, the point source or sink, originally located at coordinate z_k, is rotated by $k(z)$ and then mapped elsewhere in the complex plane by the mapping $h(z)$.

Next, the first difference with Section E1 comes to light: the point source/sink, after the mapping $h(z)$ is applied, has an angle δ_k with respect to the origin. Therefore, the next transformation has to be a rotation of angle δ_k instead of $\alpha-\beta$ (Figs E1c and d). We let Matlab compute the angle of each point source/sink with respect to the origin at this stage, given by $\delta_k = \text{angle}[k(h(z_k))]$, and use this angle in the third conformal mapping $g(z)$. However, as for each point source/sink this angle is unique, the conformal mapping for each point source/sink is uniquely given by:

$$g_k(z) = \mathrm{e}^{-i\delta_k} z. \tag{E8}$$

The fourth conformal mapping collapses the circle into a fault, denoted by $f(z)$. Next we combine the conformal mapping result with the complex potential for a point source/sink, instead of that of a uniform far-field flow. This is the second difference with Section E1, and its complex potential reads:

$$\Omega(z) = m^* \cdot \log(z - z_k). \tag{E9}$$

The complex potential for n point sources/sinks, using the four conformal mappings and expression (E9), is then given by:

$$\Omega(z) = \sum_{k=1}^{n} m_k \log(k(h(g_k(f(z)))) - k(h(g_k(f(z_s))))). \tag{E10}$$

Differentiating eq. (E10) with respect to z and simplifying leads to the following expression for the velocity field for an arbitrary (finite) number, n, of sources and sinks in the presence of an impermeable fault represented by a straight line of half length, a, tilted at angle β and mapping angle δ^k (defined in the 2nd paragraph of this section):

$$V(z) = \sum_{k=1}^{n} m_k \frac{\cos(\delta_k) - i \sin(\delta_k) \frac{1}{\sqrt{1 - \frac{e^{2i\beta} a^2}{z^2}}}}{\left(\cos(\delta_k) - i \sin(\delta_k)\sqrt{1 - \frac{e^{2i\beta} a^2}{z^2}}\right) z - \left(\cos(\delta_k) - i \sin(\delta_k)\sqrt{1 - \frac{e^{2i\beta} a^2}{z_k^2}}\right) z_k}. \tag{E11}$$

In the above formula, (E11), the fault still has its centre located at the origin. Placing the centre of the impermeable fault at z_{if} is accomplished by replacing each z and z_k by $z - z_{if}$ and $z_k - z_{if}$, respectively.